Accurate Cell-Centered Discretizations for Modeling Multiphase Flow in Porous Media on General Hexahedral and Simplicial Grids

Mary F. Wheeler, SPE, and **Guangri Xue,** SPE, University of Texas and Shell International Exploration and Production, and **Ivan Yotov,** University of Pittsburgh

Summary

We introduce an accurate cell-centered method for modeling Darcy flow on general quadrilateral, hexahedral, and simplicial grids. We refer to these discretizations as the multipoint-flux mixed-finite-element (MFMFE) method. The MFMFE method is locally conservative with continuous fluxes and can be viewed within a variational framework as a mixed finite-element method with special approximating spaces and quadrature rules. We study two versions of the method: with a symmetric quadrature rule on smooth grids and a nonsymmetric quadrature rule on rough grids. The framework allows for handling hexahedral grids with nonplanar faces defined by trilinear mappings from the reference cube. Moreover, the MFMFE method allows for local elimination of the velocity, which leads to a cell-centered pressure system. Theoretical and numerical results demonstrate first-order convergence on rough grids. Second-order superconvergence is observed on smooth grids. We also discuss a new splitting scheme for modeling multiphase flows that can treat higher-order transport discretizations for saturations. We apply the MFMFE method to obtain physically consistent approximations to the velocity and a reference pressure on quadrilateral or hexahedral grids, and a discontinuous Galerkin method for saturations. For higher-order saturations, we propose an efficient post-processing technique that gives accurate velocities in the interior of the gridblocks. Computational results are provided for flow in highly heterogeneous reservoirs, including different capillary pressures arising from different rock types.

Introduction

Geological media such as aquifers and petroleum reservoirs exhibit a high level of spatial variability at a multiplicity of scales, from the size of individual grains or pores, to facies, stratigraphic, and hydrologic units, up to the sizes of formations. In spite of its importance to a number of scientific disciplines—including the management and protection of groundwater resources, the reposition of nuclear wastes, the recovery of hydrocarbons, and the sequestration of excessive carbon—understanding physical flow and chemical reactions in heterogeneous geological media and their interplay remains a challenge. Moreover, in modeling geological systems, different physical processes need to be considered on different spatial and temporal scales, and may require different models and data. The spatial variability in the physical and geochemical properties of formations, together with measurement limitations, leads to uncertainty in describing medium properties, which in turn motivates the need for stochastic treatment of flow and reactive transport in such media. Thus, in modeling complex flow processes in porous media, it is essential for one to be able to apply accurate and efficient algorithms that can be enhanced to treat multiscale and stochastic models.

This paper (SPE 141534) was accepted for presentation at the SPE Reservoir Simulation Symposium on Improved Oil Recovery, The Woodlands, Texas, USA, 21–23 February 2011, and revised for publication. Original manuscript received for review 13 December 2010. Revised manuscript received for review 1 September 2011. Paper peer approved 7 November 2011.

In this paper, we discuss the development of a family of numerical schemes for modeling Darcy flow—the MFMFE methods. The MFMFE methods allow for an accurate and efficient treatment of irregular geometries and heterogeneities such as faults, layers, and pinchouts that require highly distorted grids and discontinuous coefficients. More precisely, these schemes are shown to be cell-centered discretizations, and to have convergent pressures and velocities on general hexahedral and simplicial grids.

The development of the MFMFE methods has been motivated by the multipoint-flux approximation (MPFA) methods (Aavatsmark 2002; Aavatsmark et al. 1998a; Edwards and Rogers 1998; Edwards 2002). In the MPFA finite-volume framework, subedge (subface) fluxes are introduced, which allows for local flux elimination and reduction to a cell-centered scheme. Similar elimination is achieved in the MFMFE variational framework, by employing appropriate finite-element spaces and special quadrature rules. Our approach is based on the BDM_1 (Brezzi et al. 1985) or the $BDDF_1$ (Brezzi et al. 1987) spaces with a trapezoidal quadrature rule applied on the reference element [see also Wheeler and Yotov (2006), Ingram et al. (2010), Wheeler et al. (2012b)]. We refer to Brezzi et al. (2006) for a similar approach on simplicial grids, as well as to Klausen and Winther (2006a, b) for a related work on quadrilateral grids using a broken Raviart-Thomas space, and to Aavatsmark et al. (2007) and Klausen et al. (2008) for papers using both approaches. There are also papers studying connections between the MPFA method and the lowest-order Raviart-Thomas RT_0 mixed-finite-element method. In Vohralík (2006), it is shown that on triangles the latter can be reduced to a nonsymmetric MPFA method without numerical quadrature. In Younes and Fontaine (2008), this method is compared numerically to our method from Wheeler and Yotov (2006) based on BDM_1 spaces and numerical quadrature, which leads to a symmetric and positive definite (SPD) formulation [see also Friis et al. (2008) for a related SPD finite-volume formulation on triangles]. On quadrilaterals, connections between the MPFA method and the RT_0 mixed-finite-element method with quadrature are investigated in Edwards (2002) and Edwards and Pal (2008).

We remark that because the MFMFE methods can be viewed in a variational framework as mixed finite elements, multiscale and multiphysics extensions such as the mortar mixed-finite-element methods (Arbogast et al. 2000, 2007; Wheeler et al. 2012c) and the enhanced-velocity method (Wheeler et al. 2002) allow for multiscale approximations, treatment of nonmatching grids, and coupling of different numerical algorithms and different physics in adjacent subdomains. The multiblock variational framework is useful in designing optimal parallel solvers that use efficient interface multiscale bases as interface preconditioners and subdomain solvers such as algebraic multigrid. These approaches have also been shown to be convergent and efficient when applying stochastic methods for uncertainty analyses (Ganis and Yotov 2009; Wheeler et al. 2011) and applying the MFMFE methods for multiscale modeling of nonlinear-flow problems in porous media (Wheeler et al. 2010a).

In this paper, we illustrate the behavior of the MFMFE method on quadrilateral and hexahedral grids applied to modeling single-phase and multiphase flow in porous media. Hexahedral grids are typically

encountered in geological models and can represent highly irregular geometries with fewer elements than tetrahedral grids. In the case of steady single-phase Darcy flow, we present examples that indicate first-order convergence of the face fluxes on rough grids and second-order convergence on smooth grids. We also show that an effective post-processing procedure can be employed that gives first-order velocities in the element interior. The variational formulation of the MFMFE method allows one to use *a posteriori* error estimates developed for mixed-finite-element-type discretizations (Pencheva et al. 2010) in adaptive mesh-refinement simulations. We present an example illustrating the effectiveness of such an estimator.

We next extend the MFMFE method to single-phase, slightly compressible Darcy flow and perform a grid refinement study that confirms convergence of the method for this nonlinear time-dependent problem. We also illustrate the flexibility of the MFMFE method to model realistic subsurface geometries by presenting a simulation on the reservoir from the Brugge benchmark project (Peters et al. 2010).

Finally, we develop a splitting scheme for two-phase flow in porous media that allows us to apply the MFMFE method for the pressure equation and a discontinuous Galerkin or a finite-volume method for the saturation equation [see also Hoteit and Firoozabadi (2008) and Sun and Wheeler (2011)* for related work on coupled RT_0 mixed finite elements and discontinuous Galerkin]. The postprocessing procedure mentioned previously provides accurate velocities in the interior of the gridblocks that are needed for second-order approximation of the saturations. The reader is referred to Aavatsmark et al. (1998b) and Edwards (2006) for related approaches to modeling multiphase Darcy flow using control volume discretizations. We present two-phase flow simulations for highly heterogeneous reservoirs, as well as for coupled rock types with different capillary pressures.

The remainder of the paper is organized as follows: Formulation of the MFMFE method, theoretical convergence, and computational results for single-phase Darcy flow are described in the next section. Subsequent sections are devoted to extensions of the MFMFE approach to slightly compressible single-phase flow and multiphase flow, respectively, before conclusions are presented in a final section.

Accurate Cell-Centered Discretizations on Hexahedral and Simplicial Grids

Consider a single-phase Darcy flow on a domain $\Omega \subset \mathbb{R}^d$, $d = 2, 3$, with a Lipschitz continuous boundary

$$\mathbf{u} = -K\nabla p \text{ in } \Omega, \quad \ldots\ldots\ldots\ldots\ldots\ldots\ldots\ldots (1)$$

$$\nabla \cdot \mathbf{u} = f \text{ in } \Omega, \quad \ldots\ldots\ldots\ldots\ldots\ldots\ldots\ldots (2)$$

$$p = 0 \text{ on } \partial\Omega, \quad \ldots\ldots\ldots\ldots\ldots\ldots\ldots\ldots (3)$$

where $\mathbf{u}$ is the Darcy velocity, p is the pressure, and K is a symmetric, uniformly positive definite tensor with $L^\infty(\Omega)$ components representing the rock permeability divided by the fluid viscosity. The choice of homogeneous pressure boundary conditions is made for simplicity of the presentation; other boundary conditions can also be treated. The weak formulation of Eqs. 1 through 3 reads: find $\mathbf{u} \in H(\mathbf{div}; \Omega)$ and $p \in L^2(\Omega)$, such that

$$(K^{-1}\mathbf{u}, \mathbf{v}) - (p, \nabla \cdot \mathbf{v}) = 0, \ \forall \mathbf{v} \in H(\mathbf{div}; \Omega), \quad \ldots\ldots\ldots (4)$$

$$(\nabla \cdot \mathbf{u}, w) = (f, w), \ \forall w \in L^2(\Omega), \quad \ldots\ldots\ldots\ldots\ldots (5)$$

where $H(\mathbf{div}; \Omega) := \{\mathbf{v} \in (L^2(\Omega))^d : \nabla \cdot \mathbf{v} \in L^2(\Omega)\}$ and $(\cdot, \cdot)$ denotes the inner product in $L^2(\Omega)$.

Definition of the MFMFE Method. MFMFE methods have been developed and analyzed in Wheeler and Yotov (2006), Ingram et al. (2010), and Wheeler et al. (2012b, c) for simplicial, quadrilateral, and hexahedral grids. The method is defined as follows: find $\mathbf{u}_h \in V_h$ and $p_h \in W_h$ such that

$$(K^{-1}\mathbf{u}_h, \mathbf{v})_Q - (p_h, \nabla \cdot \mathbf{v}) = 0, \ \forall \mathbf{v} \in V_h, \quad \ldots\ldots\ldots\ldots (6)$$

$$(\nabla \cdot \mathbf{u}_h, w) = (f, w), \ \forall w \in W_h, \quad \ldots\ldots\ldots\ldots\ldots (7)$$

There are two key ingredients in the method. The first is an appropriate choice of mixed-finite-element spaces (V_h and W_h) and degrees of freedom. The second is a specific choice of the numerical integration rules for $(\cdot, \cdot)_Q$ in Eq. 6. These two choices allow for a flux variable defined at a vertex to be expressed by gridblock pressures surrounding the vertex. This results in a nine-point or 27-point pressure stencil in logically rectangular 2D or 3D grids.

The quadrature rule (Eq. 15) can be symmetric or nonsymmetric. We call the method a symmetric or nonsymmetric MFMFE method based on the quadrature rule. The symmetric and nonsymmetric MFMFE methods are closely related to the reference and physical space MPFA methods, respectively (Aavatsmark 2002; Aavatsmark et al. 2007; Edwards and Pal 2008). On smooth hexahedral grids, both the symmetric and nonsymmetric MFMFE methods give first-order accurate velocities and pressures, as well as second-order accurate face fluxes and pressures at the cell centers (Wheeler and Yotov 2006; Ingram et al. 2010; Wheeler et al. 2012b). On highly distorted hexahedral grids with nonplanar faces (Wheeler et al. 2012b), the convergence of the symmetric MFMFE can deteriorate while the nonsymmetric MFMFE still gives a first-order accuracy. On simplicial grids, the two quadrature rules in Eq. 15 are the same because the Jacobian is a constant matrix, and the method gives first-order accuracy for the velocity and pressure. The nonsymmetric quadrature rule was first proposed in Klausen and Winther (2006b) for quadrilateral grids.

In the remaining subsection, we discuss the two ingredients in details.

Finite-Element Spaces. Let Ω be a polyhedral domain partitioned into a union of finite elements (gridblocks) of characteristic size h. The elements can be triangles or quadrilaterals in 2D, or tetrahedra or hexahedra in 3D. In the following, we present the method in 3D. Let us denote the partition by $\mathcal{T}_h$ and assume that it is shape-regular and quasiuniform (Ciarlet 2002). The velocity and pressure finite-element spaces on any physical gridblock E are defined, respectively, by the Piola transformation,

$$\mathbf{v} \leftrightarrow \hat{\mathbf{v}} : \mathbf{v} = \frac{1}{J_E} DF_E \hat{\mathbf{v}} \circ F_E^{-1},$$

and the scalar transformation,

$$w \leftrightarrow \hat{w} : w = \hat{w} \circ F_E^{-1},$$

where $\hat{E}$ is the reference cube or tetrahedron; F_E denotes a trilinear mapping or an affine mapping from $\hat{E}$ to E in the case of hexahedral and simplicial grids, respectively; DF_E is the Jacobian of F_E; and J_E is its determinant. The Piola transformation preserves the normal components of the vectors. The finite-element spaces V_h and W_h on $\mathcal{T}_h$ are given by

$$V_h = \{\mathbf{v} \in H(\mathbf{div}; \Omega) : \mathbf{v}|_E \leftrightarrow \hat{\mathbf{v}}, \ \hat{\mathbf{v}} \in \hat{V}(\hat{E}), \ \forall E \in \mathcal{T}_h\}$$
$$W_h = \{w \in L^2(\Omega) : w|_E \leftrightarrow \hat{w}, \ \hat{w} \in \hat{W}(\hat{E}), \ \forall E \in \mathcal{T}_h\}$$
$$\ldots\ldots\ldots\ldots\ldots\ldots\ldots\ldots (8)$$

where $\hat{V}(\hat{E})$ and $\hat{W}(\hat{E})$ are finite-element spaces on the reference element $\hat{E}$.

On the reference cube, the spaces are defined by enhancing the $BDDF_1$ spaces (Ingram et al. 2010):

$$\begin{aligned}\hat{V}(\hat{E}) = {} & BDDF_1(\hat{E}) + r_2 \text{curl}(0, 0, \hat{x}^2\hat{z})^T \\ & + r_3 \text{curl}(0, 0, \hat{x}^2\hat{y}\hat{z})^T \\ & + s_2 \text{curl}(\hat{x}\hat{y}^2, 0, 0)^T \\ & + s_3 \text{curl}(\hat{x}\hat{y}^2\hat{z}, 0, 0)^T \\ & + t_2 \text{curl}(0, \hat{y}\hat{z}^2, 0)^T \\ & + t_3 \text{curl}(0, \hat{x}\hat{y}\hat{z}^2, 0)^T, \\ \hat{W}(\hat{E}) = {} & P_0(\hat{E}),\end{aligned} \quad \ldots\ldots\ldots\ldots (9)$$

* Private communication.

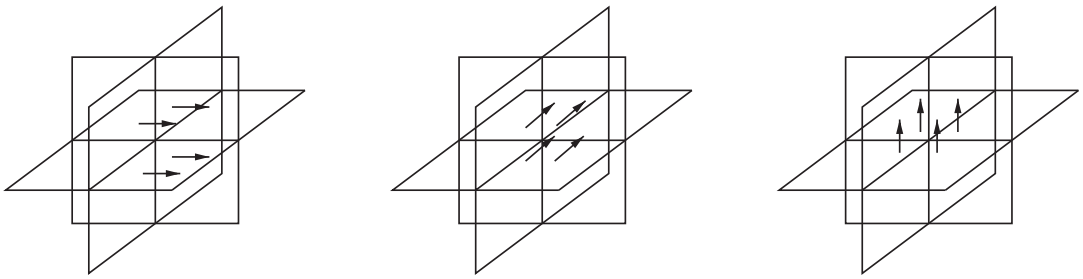

Fig. 1—Interactions of the velocity DOFs in the MFMFE method.

where the $\mathrm{BDDF}_1(\hat{E})$ space is defined as (Brezzi et al. 1987)

$$\begin{aligned} BDDF_1(\hat{E}) = P_1(\hat{E})^3 &+ r_0\mathrm{curl}(0,0,\hat{x}\hat{y}\hat{z})^T \\ &+ r_1\mathrm{curl}(0,0,\hat{x}\hat{y}^2)^T \\ &+ s_0\mathrm{curl}(\hat{x}\hat{y}\hat{z},0,0)^T, \\ &+ s_1\mathrm{curl}(\hat{y}\hat{z}^2,0,0)^T \\ &+ t_0\mathrm{curl}(0,\hat{x}\hat{y}\hat{z},0)^T \\ &+ t_1\mathrm{curl}(0,\hat{x}^2\hat{z},0)^T. \end{aligned} \quad \ldots\ldots\ldots (10)$$

In these equations, $r_i, s_i, t_i (i = 0, \ldots, 3)$ are real constants, P_k denotes polynomials of degree at most k, and $(\hat{x}, \hat{y}, \hat{z})^T$ denotes a point in the reference element. The enhancement of the BDDF_1 space is needed to obtain a space with four degrees of freedom per face, rather than three in the original formulation. This allows one to associate a degree of freedom with each vertex of the face, which is needed in the reduction to a cell-centered pressure stencil, as described later in this section.

On the reference tetrahedron, the spaces are chosen as the BDM_1 spaces (Brezzi et al. 1985):

$$\begin{aligned} \hat{V}(\hat{E}) &= P_1(\hat{E})^3, \\ \hat{W}(\hat{E}) &= P_0(\hat{E}). \end{aligned} \quad \ldots\ldots\ldots\ldots\ldots\ldots\ldots (11)$$

On the reference cube or tetrahedron, there are four or three degrees of freedom (DOFs) per face, respectively. The DOFs are chosen to be the normal components at the vertices. This choice of DOF guarantees continuity of the normal component of the velocity vector across element faces, which is needed for an $H(\mathbf{div};\Omega)$-conforming velocity space, as required by Eq. 8.

A Quadrature Rule. The integration on a physical element is performed by mapping to the reference element and choosing a quadrature rule on $\hat{E}$. Using the Piola transformation, we write $(K^{-1}\cdot,\cdot)$ in Eq. 4 as

$$\begin{aligned} (K^{-1}\mathbf{q},\mathbf{v})_E &= \left(\frac{1}{J_E}DF_E^T K^{-1}(F_E(\hat{x}))DF_E\hat{\mathbf{q}},\hat{\mathbf{v}}\right)_{\hat{E}} \\ &\equiv (\mathcal{M}_E\hat{\mathbf{q}},\hat{\mathbf{v}})_{\hat{E}}, \end{aligned}$$

where

$$\mathcal{M}_E = \frac{1}{J_E}DF_E^T K^{-1}(F_E(\hat{x}))DF_E. \quad \ldots\ldots\ldots\ldots\ldots (12)$$

Define a perturbed $\widetilde{\mathcal{M}}_E$ as

$$\widetilde{\mathcal{M}}_E = \frac{1}{J_E}DF_E^T(\hat{\mathbf{r}}_{c,\hat{E}})\overline{K}_E^{-1}DF_E, \quad \ldots\ldots\ldots\ldots\ldots (13)$$

where $\hat{\mathbf{r}}_{c,\hat{E}}$ is the centroid of $\hat{E}$ and $\overline{K}_E$ denotes the mean of K on E. In addition, denote the trapezoidal rule on $\hat{E}$ by $\mathrm{Trap}(\cdot,\cdot)_{\hat{E}}$:

$$\mathrm{Trap}(\hat{\mathbf{q}},\hat{\mathbf{v}})_{\hat{E}} \equiv \frac{|\hat{E}|}{k}\sum_{i=1}^{k}\hat{\mathbf{q}}(\hat{\mathbf{r}}_i)\cdot\hat{\mathbf{v}}(\hat{\mathbf{r}}_i), \quad \ldots\ldots\ldots\ldots (14)$$

where $\{\hat{\mathbf{r}}_i\}_{i=1}^k$ are the vertices of $\hat{E}$.

The symmetric quadrature rule is based on the original $\mathcal{M}_E$, while the nonsymmetric one is based on the perturbed $\widetilde{\mathcal{M}}_E$. The quadrature rule on an element E is defined as

$$(K^{-1}\mathbf{q},\mathbf{v})_{Q,E} \equiv \begin{cases} \mathrm{Trap}(\mathcal{M}_E\hat{\mathbf{q}},\hat{\mathbf{v}})_{\hat{E}} = \frac{|\hat{E}|}{k}\sum_{i=1}^{k}\mathcal{M}_E(\hat{\mathbf{r}}_i)\hat{\mathbf{q}}(\hat{\mathbf{r}}_i)\cdot\hat{\mathbf{v}}(\hat{\mathbf{r}}_i), \\ \qquad\qquad \text{symmetric}, \\ \mathrm{Trap}\left(\widetilde{\mathcal{M}}_E\hat{\mathbf{q}},\hat{\mathbf{v}}\right)_{\hat{E}} = \frac{|\hat{E}|}{k}\sum_{i=1}^{k}\widetilde{\mathcal{M}}_E(\hat{\mathbf{r}}_i)\hat{\mathbf{q}}(\hat{\mathbf{r}}_i)\cdot\hat{\mathbf{v}}(\hat{\mathbf{r}}_i), \\ \qquad\qquad \text{nonsymmetric}. \end{cases} \quad \ldots\ldots\ldots\ldots\ldots (15)$$

Mapping back to the physical element E, we have the quadrature rule on E as

$$(K^{-1}\mathbf{q},\mathbf{v})_{Q,E} \equiv \begin{cases} \frac{1}{k}\sum_{i=1}^{k}J_E(\hat{\mathbf{r}}_i)K_E^{-1}\mathbf{q}(\mathbf{r}_i)\cdot\mathbf{v}(\mathbf{r}_i), \\ \qquad\qquad \text{symmetric}, \\ \frac{1}{k}\sum_{i=1}^{k}J_E(\hat{\mathbf{r}}_i)\left(DF_E^{-1}\right)^T(\hat{\mathbf{r}}_i)DF_E^T\left(\hat{r}_{c,\hat{E}}\right)\overline{K}_E^{-1}\mathbf{q}(\mathbf{r}_i)\cdot\mathbf{v}(\mathbf{r}_i), \\ \qquad\qquad \text{nonsymmetric}. \end{cases} \quad \ldots\ldots\ldots\ldots\ldots (16)$$

The nonsymmetric quadrature rule has certain critical properties on the physical elements that lead to a convergent method on rough hexahedra (Wheeler et al. 2012b).

The global quadrature rule on Ω is then given as

$$(K^{-1}\mathbf{q},\mathbf{v})_Q \equiv \sum_{E\in\mathcal{T}_h}(K^{-1}\mathbf{q},\mathbf{v})_{Q,E}.$$

Reduction to a Cell-Centered Pressure System. The choice of trapezoidal quadrature rule implies that on each element, the velocity DOFs associated with a vertex become decoupled from the rest of the DOFs. As a result, the assembled velocity mass matrix in Eq. 6 has a block-diagonal structure with one block per grid vertex. The dimension of each block equals the number of velocity DOFs associated with the vertex. For example, this dimension is 12 for logically rectangular hexahedral grids (see **Fig. 1**). Inverting each local block in the mass matrix in Eq. 6 allows for expressing the velocity DOF associated with a vertex in terms of the pressures at the centers of the elements that share the vertex (there are eight such elements in Fig. 1). Substituting these expressions into the mass-conservation equation (Eq. 7) leads to a cell-centered system for the pressures. The stencil is 27 points on logically rectangular hexahedral grids. The local linear systems and the resulting global pressure system are positive-definite and therefore invertible for the symmetric MFMFE method and, under a mild restriction on the shape regularity of the grids and/or the anisotropy of the permeability, for the nonsymmetric MFMFE method; see Eq. 21. The reader is referred to Wheeler and Yotov (2006), Ingram et al. (2010), and Wheeler et al. (2010b) for further details on the reduction to a cell-centered pressure system.

Convergence of the Symmetric MFMFE. We first introduce some notations. Let $W_{\mathcal{T}_h}^{k,\infty}$ consist of functions ϕ such that $\phi|_E \in W^{k,\infty}(E)$ for all $E \in \mathcal{T}_h$. Here, k is a multiindex with integer components and $W^{k,\infty}(E)$ denotes the Sobolev space of functions whose derivatives of order k belong to $L^\infty(E)$. In addition, let

$\|\cdot\|_k$ be the norm in the Hilbert space $H^k(\Omega)$ with functions whose derivatives of order k belong to $L^2(\Omega)$. The norm in $L^2(\Omega)$ is denoted by $\|\cdot\|$. Let $X \lesssim (\gtrsim) Y$ denote that there exists a constant C, independent of the mesh size h, such that $X \leq (\geq) CY$. The notation $X \approx Y$ means that both $X \lesssim Y$ and $X \gtrsim Y$ hold.

On simplicial grids, h^2-perturbed parallelograms, and h^2-perturbed parallelepipeds, the following convergence results have been established for the symmetric MFMFE method.

Theorem 1 (Wheeler and Yotov 2006; Ingram et al. 2010). If $K^{-1} \in W^{1,\infty}_{\mathcal{T}_h}$, then, the velocity $\mathbf{u}_h$ and pressure p_h of the symmetric MFMFE method (Eqs. 6 and 7) satisfy

$$\|\mathbf{u} - \mathbf{u}_h\| \lesssim h\|\mathbf{u}\|_1, \quad \ldots\ldots\ldots\ldots\ldots\ldots\ldots\ldots (17)$$

$$\|\nabla \cdot (\mathbf{u} - \mathbf{u}_h)\| \lesssim h\|\nabla \cdot \mathbf{u}\|_1, \quad \ldots\ldots\ldots\ldots\ldots\ldots (18)$$

$$\|p - p_h\| \lesssim h(\|\mathbf{u}\|_1 + \|p\|_1). \quad \ldots\ldots\ldots\ldots\ldots\ldots (19)$$

Convergence of the Nonsymmetric MFMFE. On simplicial grids, h^2-perturbed parallelograms, and h^2-perturbed parallelepipeds, the nonsymmetric MFMFE method has same order of accuracy as the symmetric method. In addition, the nonsymmetric method has first-order convergence for the velocity and pressure on general quadrilaterals and for the face flux and pressure on general hexahedra with nonplanar faces.

For the analysis of the nonsymmetric MFMFE method, we require some properties of the bilinear form $(K^{-1}\cdot,\cdot)_Q$ defined on the space V_h. Note that

$$(K^{-1}\mathbf{q}, \mathbf{v})_Q = \sum_{E \in \mathcal{T}_h} (K^{-1}\mathbf{q}, \mathbf{v})_{Q,E} = \sum_{c \in \mathcal{C}_h} \mathbf{v}_c^T \mathbf{M}_c \mathbf{q}_c, \quad \ldots\ldots (20)$$

where $\mathcal{C}_h$ denotes the set of corner or vertex points in $\mathcal{T}_h$, $\mathbf{v}_c := \{(\mathbf{v} \cdot \mathbf{n}_e)(\mathbf{x}_c)\}_{e=1}^{n_c}$, $\mathbf{x}_c$ is the coordinate vector of Point c, and n_c is the number of faces (or edges in 2D) that share the vertex Point c.

Lemma 1 (Wheeler et al. 2012b). Assume that $\mathbf{M}_c$ is uniformly positive definite for all $c \in \mathcal{C}_h$:

$$h^d \xi^T \xi \lesssim \xi^T \mathbf{M}_c \xi, \ \forall \xi \in \mathbb{R}^{n_c}. \quad \ldots\ldots\ldots\ldots\ldots (21)$$

Then the bilinear form $(K^{-1}\cdot,\cdot)_Q$ is coercive in V_h and induces a norm in V_h equivalent to the L^2-norm:

$$(K^{-1}\mathbf{v}, \mathbf{v})_Q \approx \|\mathbf{v}\|^2, \ \forall \mathbf{v} \in V_h. \quad \ldots\ldots\ldots\ldots\ldots (22)$$

If in addition

$$\xi^T \mathbf{M}_c^T \mathbf{M}_c \xi \lesssim h^{2d} \xi^T \xi, \ \forall \xi \in \mathbb{R}^{n_c}, \quad \ldots\ldots\ldots\ldots\ldots (23)$$

then the following Cauchy-Schwarz type inequality holds:

$$(K^{-1}\mathbf{q}, \mathbf{v})_Q \lesssim \|\mathbf{q}\|\|\mathbf{v}\|, \ \forall \mathbf{q}, \mathbf{v} \in V_h, \quad \ldots\ldots\ldots\ldots\ldots (24)$$

Conditions in Eqs. 21 and 23 impose certain restrictions on the element geometry and the anisotropy of the permeability tensor K (Klausen and Winther 2006b; Lipnikov et al. 2009). We explore these restrictions in our numerical experiments.

Theorem 2 (Wheeler et al. 2012b). Let $K \in W^{1,\infty}_{\mathcal{T}_h}(\Omega)$ and $K^{-1} \in W^{0,\infty}(\Omega)$. If Eqs. 21 and 23 hold, then the velocity $\mathbf{u}_h$ and the pressure p_h of the nonsymmetric MFMFE method in Eqs. 6 and 7 satisfy

$$\|\Pi\mathbf{u} - \mathbf{u}_h\| + \|Q_h p - p_h\| \lesssim h(|\mathbf{u}|_1 + \|p\|_2), \quad \ldots\ldots\ldots (25)$$

where Π is the canonical interpolation operator onto V_h and Q_h is the L^2-orthogonal projection onto W_h.

This result further implies convergence of the computed normal velocity to the true normal velocity on the element faces. First, define a norm for vectors in Ω based on the normal components on the faces of $\mathcal{T}_h$:

$$\|\mathbf{v}\|^2_{\mathcal{F}_h} := \sum_{E \in \mathcal{T}_h} \sum_{e \in \partial E} \frac{|E|}{|e|} \|\mathbf{v} \cdot \mathbf{n}_e\|^2_e, \quad \ldots\ldots\ldots\ldots\ldots (26)$$

where $|E|$ is the volume of E and $|e|$ is the area of e. This norm gives an appropriate scaling of $|\Omega|^{1/2}$ for a unit vector.

Theorem 3 (Wheeler et al. 2012b). Let $K \in W^{1,\infty}_{\mathcal{T}_h}(\Omega)$ and $K^{-1} \in W^{0,\infty}_{\mathcal{T}_h}(\Omega)$. If Eqs. 21 and 23 hold, then the velocity $\mathbf{u}_h$ of the nonsymmetric MFMFE method in Eqs. 6 and 7 satisfies

$$\|\mathbf{u} - \mathbf{u}_h\|_{\mathcal{F}_h} \lesssim h(\|\mathbf{u}\|_1 + \|p\|_2). \quad \ldots\ldots\ldots\ldots\ldots (27)$$

Numerical experiments confirming the theories are presented in the Convergence Tests subsection.

Accurate Velocity Inside Hexahedra by Post-Processing. On smooth hexahedra, the interpolation error $\|\mathbf{u} - \Pi\mathbf{u}\|$ is first-order convergent (Ingram et al. 2010), which gives first-order accuracy of $\|\mathbf{u} - \mathbf{u}_h\|$ also. On highly distorted hexahedra, the interpolation error $\|\mathbf{u} - \Pi\mathbf{u}\|$ is not convergent (Naff et al. 2002; Wheeler et al. 2012a). A numerical example in the Convergence Tests subsection indicates that in such a case, $\|\mathbf{u} - \mathbf{u}_h\|$ does not have first-order convergence. The nonsymmetric MFMFE method gives accurate face velocities on general hexahedral grids—namely, $\|\mathbf{u} - \mathbf{u}_h\|_{\mathcal{F}_h}$ has first-order convergence.

In multiphase-flow simulations, if one uses a finite-volume method with a piecewise constant approximation for the saturation equation, accurate face velocities are sufficient to give first-order accurate saturations. For higher-order methods, for the saturation equation such as the discontinuous Galerkin method with piecewise linears, one needs accurate velocity in the interior of the gridblocks—namely, the accuracy of $\|\mathbf{u} - \mathbf{u}_h\|$ (Lamine and Edwards 2010). To achieve first-order accuracy for the velocity inside hexahedra, we have introduced a post-processing technique (Wheeler et al. 2012a). The extra computational cost is very small, solving a 3×3 local system in each gridblock.

Post-Processing. Theorem 3 states that the nonsymmetric MFMFE method gives first-order accurate face velocities. We use these face velocities as Neumann boundary conditions and solve Eqs. 1 and 2 in each hexahedron E:

$$\widetilde{\mathbf{u}} = -K\nabla\widetilde{p}, \text{ in } E, \quad \ldots\ldots\ldots\ldots\ldots\ldots (28)$$

$$\nabla \cdot \widetilde{\mathbf{u}} = f, \text{ in } E, \quad \ldots\ldots\ldots\ldots\ldots\ldots (29)$$

$$\widetilde{\mathbf{u}} \cdot \mathbf{n}_E = \mathbf{u}_h \cdot \mathbf{n}_E, \text{ on } \partial E. \quad \ldots\ldots\ldots\ldots\ldots (30)$$

This problem is solvable because of

$$\int_E f dx = \int_{\partial E} \mathbf{u}_h \cdot \mathbf{n}_E ds, \quad \ldots\ldots\ldots\ldots\ldots (31)$$

which follows from the local conservation property (Eq. 7) of the MFMFE method. We use the following mixed-finite-element method to solve Eqs. 28 through 30.

Finite-Element Spaces on Hexahedra. The global finite-element spaces are defined as in Eq. 8. It is sufficient to specify the finite-element spaces on the reference element $\hat{E}$. Choose the velocity space $\hat{V}^*(\hat{E})$ as (Wheeler et al. 2012a)

$$\begin{aligned}\hat{V}^*(\hat{E}) = \mathrm{BDDF}_1(\hat{E}) \quad & + \frac{R_1}{2}\mathrm{curl}(\hat{x}\hat{y}^2, 0, 0)^T + \frac{R_2}{2}\mathrm{curl}(0, \hat{y}\hat{z}^2, 0)^T \\ & + \frac{R_3}{2}\mathrm{curl}(0, 0, \hat{x}^2\hat{z})^T + S_1\mathrm{curl}(\hat{x}\hat{y}^2\hat{z}, 0, 0)^T \\ & + S_2\mathrm{curl}(0, \hat{x}\hat{y}\hat{z}^2, 0)^T + S_3\mathrm{curl}(0, 0, \hat{x}^2\hat{y}\hat{z})^T \\ & + \frac{H_1}{2}\mathrm{curl}(\hat{y}^2\hat{z}^2, 0, 0)^T + \frac{H_2}{2}\mathrm{curl}(0, \hat{x}^2\hat{z}^2, 0)^T \\ & + \frac{H_3}{2}\mathrm{curl}(0, 0, \hat{x}^2\hat{y}^2)^T, \quad \ldots\ldots\ldots (32)\end{aligned}$$

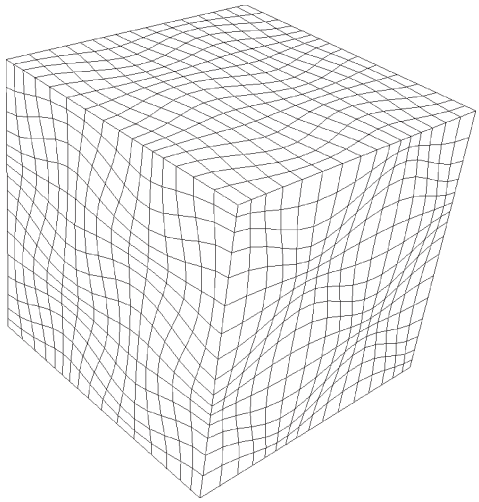

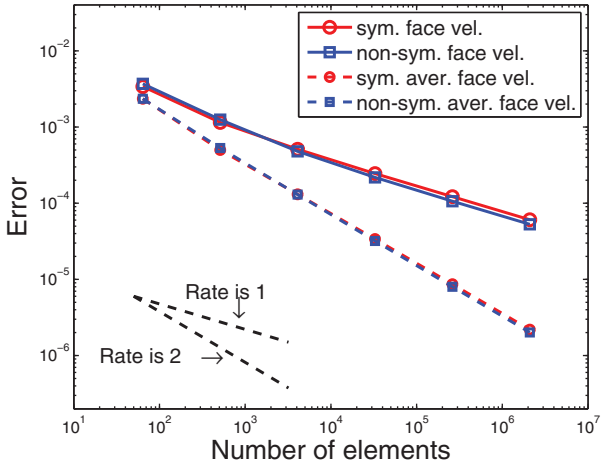

Fig. 2—Example 1: An h^2-perturbed hexahedral mesh (left), and the convergence (right) of the face-velocity error $\|\mathbf{u}-\mathbf{u}_h\|_{\mathcal{F}_h}$ and the average face-velocity error $|||\mathbf{u}-\mathbf{u}_h|||_{\mathcal{F}_h}$ for the symmetric and nonsymmetric MFMFE methods (ω=100).

where R_i, S_i, H_i, $i=1,\ldots,3$, are real constants. The DOFs for $\hat{\mathbf{u}} \in \hat{V}^*(\hat{E})$ are

- $(\hat{\mathbf{u}}\cdot\hat{\mathbf{n}},\hat{q})_{\hat{e}}, \forall \hat{q} \in Q_1(\hat{e})$
- $(\hat{\mathbf{u}},\hat{\mathbf{r}})_{\hat{E}}, \forall \hat{\mathbf{r}} \in \hat{\mathbf{R}}$, where $\hat{\mathbf{R}}$ denotes the span of the vectors:

$$\hat{\mathbf{r}}_1 := (0, 1/2-\hat{z}, \hat{y}-1/2)^T,$$
$$\hat{\mathbf{r}}_2 := (1/2-\hat{z}, 0, \hat{x}-1/2)^T,$$
$$\hat{\mathbf{r}}_3 := (1/2-\hat{y}, \hat{x}-1/2, 0)^T.$$

In addition to four velocity DOFs per face as in the space $\hat{V}(\hat{E})$ in an earlier subsection, three DOFs inside the element are added to gain accuracy in the L^2 norm. In fact, the space $\hat{V}^*(\hat{E})$ is constructed by adding one velocity DOF per face to the space developed in Falk et al. (2011). For this reason, we call our space an enhanced $\mathcal{FGM}$ space. For the pressure, the constant space $\hat{W}(\hat{E})$ is employed.

We use the enhanced $\mathcal{FGM}$ finite-element method to solve the problem in Eqs. 28 through 30: find $\mathcal{P}(\mathbf{u}_h) := \tilde{\mathbf{u}}_h \in V_h^*$ with $\tilde{\mathbf{u}}_h\cdot\mathbf{n} = \mathbf{u}_h\cdot\mathbf{n}$ on ∂E and $\tilde{p}_h \in W_h(E)$ such that

$$(K^{-1}\tilde{\mathbf{u}}_h,\mathbf{v})_E - (\tilde{p}_h, \nabla\cdot\mathbf{v})_E = 0,\ \forall \mathbf{v}\in V_{h,0}^*(E), \quad \ldots\ldots (33)$$

$$(\nabla\cdot\tilde{\mathbf{u}}_h, w)_E = (f,w)_E,\ \forall w \in W_h(E), \quad \ldots\ldots\ldots\ldots (34)$$

where

$$V_{h,0}^*(E) := \{\mathbf{v}\in V_h^*(E)\,|\,\mathbf{v}\cdot\mathbf{n}=0 \text{ on } \partial E\}. \quad \ldots\ldots\ldots (35)$$

By Eqs. 30, 31, and 35, the previous equations are equivalent to

$$(K^{-1}\tilde{\mathbf{u}}_h,\mathbf{v})_E = 0,\ \forall \mathbf{v}\in V_{h,0}^*(E), \quad \ldots\ldots\ldots\ldots\ldots (36)$$

which amounts to solving a 3×3 linear system for the three DOFs inside each hexahedral element E.

Theorem 4 (Wheeler et al. 2012a). The post-processed velocity $\mathcal{P}(\mathbf{u}_h)$ of Eqs. 33 and 34 satisfies

$$\|\mathbf{u}-\mathcal{P}(\mathbf{u}_h)\| \lesssim h(|\mathbf{u}|_1 + \|p\|_2). \quad \ldots\ldots\ldots\ldots\ldots (37)$$

Convergence Tests. We consider the problem in Eqs. 1 through 3 with a given analytical solution:

$$p(x,y,z) = x^2(x-1)^2y^2(y-1)^2z^3(1-z)^3,$$

and a full permeability tensor,

$$K = \begin{pmatrix} 2 & 1 & 1 \\ 1 & 2 & 1 \\ 1 & 1 & \omega \end{pmatrix}.$$

The computational domain is the unit cube $[0,1]^3$. We take $\omega = 10, 100, 1000$ in order to explore the limitations of the nonsymmetric MFMFE method on distorted hexahedra and highly anisotropic full-tensor permeabilities. We test both smooth and rough grids in Examples 1 and 2, described later. We observed that the coercivity condition (Eq. 21) was violated in some cases, resulting in a singular algebraic problem. For each mesh, we report results for the largest value of ω among the three tested, for which the nonsymmetric MFMFE method was positive definite. The symmetric method was coercive in all cases, but exhibited deterioration in the convergence on rough grids, as predicted by the theory of Ingram et al. (2010). There have been a number of studies in the literature on the limitations of the closely related MPFA method on anisotropic grids and permeabilities. Some modifications of the MPFA method with improved coercivity and monotonicity properties have been developed, including methods with compact stencils (Aavatsmark et al. 2008, 2010) or increased pressure support (Edwards and Zheng 2008, 2010, 2011). These approaches, as well as grid-smoothing techniques (https://www.gridpro.com/) or adaptive grid refinement (Pencheva et al. 2010) could be applied to the MFMFE method.

Example 1: Smooth Grids. We test convergence of face velocities on smooth hexahedral grids. The sequence of hexahedral meshes is generated using a smooth map of a uniform grid given by

$$x = \hat{x} + 0.03\sin(3\pi\hat{x})\cos(3\pi\hat{y})\cos(3\pi\hat{z}),$$
$$y = \hat{y} - 0.04\cos(3\pi\hat{x})\sin(3\pi\hat{y})\cos(3\pi\hat{z}),$$
$$z = \hat{z} + 0.05\cos(3\pi\hat{x})\cos(3\pi\hat{y})\sin(3\pi\hat{z}).$$

This mapping yields an h^2-parallelepiped mesh, as shown in **Fig. 2.** The face-velocity error $\|\mathbf{u}-\mathbf{u}_h\|_{\mathcal{F}_h}$ is plotted vs. the number of gridblocks for both the symmetric and the nonsymmetric MFMFE methods. As the theory predicts, both methods give first-order accuracy. In addition, we also report the convergence in the discrete flux error

$$|||\mathbf{u}-\mathbf{u}_h|||_{\mathcal{F}_h}^2 \equiv \sum_{E\in\mathcal{T}_h}\sum_{e\in\partial E}|E|\left(\frac{1}{|e|}\int_e \mathbf{u}\cdot\mathbf{n}_e - \frac{1}{|e|}\int_e \mathbf{u}_h\cdot\mathbf{n}_e\right)^2.$$

With this discrete face-velocity norm, we observe second-order superconvergence, as shown in Fig. 2. Because of the smoothness of the grid, the symmetric and the nonsymmetric MFMFE methods give very similar solution accuracy.

Example 2: Rough Grids. We test convergence of the face velocities on rough hexahedral grids. Consider a sequence of hexahedral meshes as shown in **Fig. 3.** The meshes are generated by

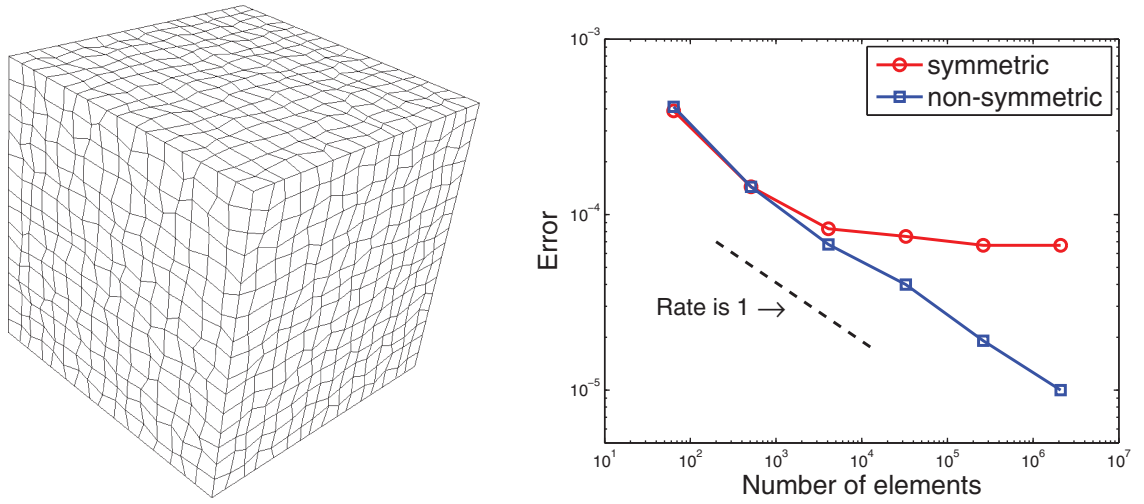

Fig. 3—Example 2: A randomly *h*-perturbed hexahedral mesh (left) and error (right) $\|\mathbf{u}-\mathbf{u}_h\|_{\mathcal{F}_h}$ in the symmetric and the nonsymmetric MFMFE methods (ω=10).

randomly perturbing each gridpoint (from uniform refinements) within a cube with edge length $0.5h$ centered at the gridpoint. This results in highly distorted nonconvex elements with nonplanar faces. We test the convergence of the face velocities of both the symmetric and the nonsymmetric MFMFE methods. In Fig. 3, we plot $\|\mathbf{u}-\mathbf{u}_h\|_{\mathcal{F}_h}$ vs. the number of gridblocks. Clearly the convergence of the symmetric method deteriorates. As Theorem 3 indicates, the face velocity of the nonsymmetric MFMFE method has first-order convergence.

Example 3: Post-Processed Velocity. We test the convergence of the post-processed cell velocity on rough hexahedral grids. Consider a sequence of hexahedral meshes as shown in **Fig. 4.** These meshes are considered in Falk et al. (2011) to find the smallest velocity space that gives first-order approximation of the canonical interpolation on a general hexahedra. We plot the following two errors, $\|\mathbf{u}-\mathbf{u}_h\|$ and $\|\mathbf{u}-\mathcal{P}(\mathbf{u}_h)\|$, with respect to the number of gridblocks. As Theorem 4 predicts, we observe first-order convergence for the post-processed velocity $\mathcal{P}(\mathbf{u}_h)$. The convergence $\|\mathbf{u}-\mathbf{u}_h\|$ deteriorates because of the missing three DOFs inside each hexahedron.

Example 4: A Posteriori Error Estimation. The MFMFE method can be used with an *a posteriori* error estimator that guides an adaptive mesh-refinement algorithm. Such a strategy leads to efficient and accurate approximations by resolving local features of the solution, such as sharp gradients or singularities, using a locally refined mesh.

We consider the *a posteriori* error estimator developed in Pencheva et al. (2010) for any locally conservative velocity field $\mathbf{u}_h$,

$$\|\mathbf{u}-\mathbf{u}_h\|_a \le \inf_{q\in H_0^1} \|\mathbf{u}_h + K\nabla q\|_a + \eta_R,$$

where $\|\mathbf{v}\|_a := (K^{-1}\mathbf{v},\mathbf{v})^{1/2}$ and $\eta_R := \left\{\sum_{E\in\mathcal{T}_h} \frac{C_P h_E^2}{c_{K,E}} \|f-\nabla\cdot\mathbf{u}_h\|_E^2\right\}^{1/2}$. This estimator is fully computable without any hidden constants. Here, C_P is the Poincaré constant with respect to the element E. For example, $C_P=\frac{1}{\pi^2}$ on simplices and rectangular parallelepipeds. $c_{K,E}$ is the smallest eigenvalue of the tensor K on E. In practice, q is chosen as the Oswald interpolation of a post-processed pressure $\widetilde{p}_h$, denoted $\mathcal{I}_{OS}(\widetilde{p}_h)$. Computation of $\widetilde{p}_h$ involves solving a small linear algebraic system in each element. Here, we test the accuracy of the error estimator by considering the same sequence of meshes as in Example 1 with a full-tensor permeability:

$$K=\begin{pmatrix} 2 & 1.25 & 1.5 \\ 1.25 & 3 & 2 \\ 1.5 & 2 & 4 \end{pmatrix},$$

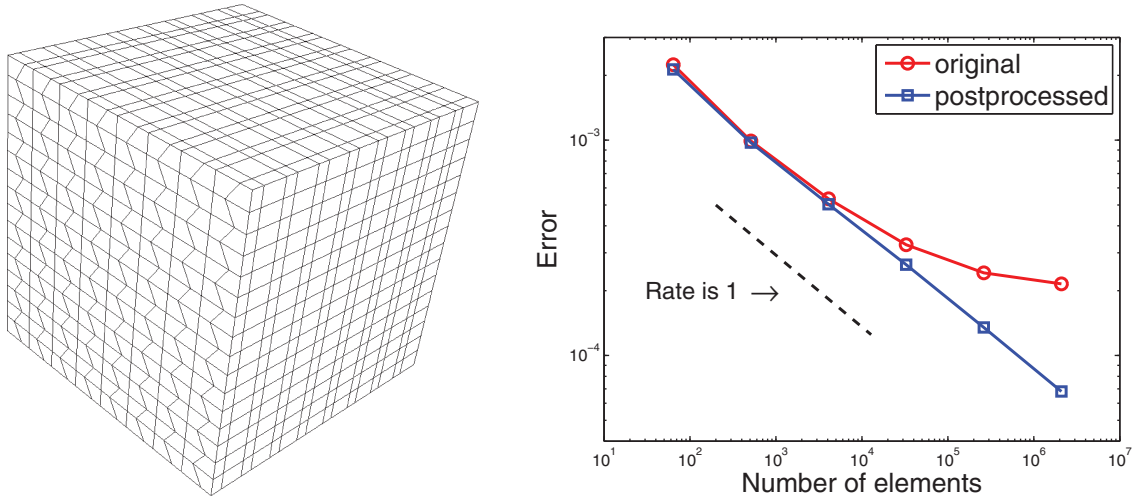

Fig. 4—Example 3: An *h*-perturbed hexahedral mesh (left) and error (right) of original $\|\mathbf{u}-\mathbf{u}_h\|_{\mathcal{F}_h}$ and post-processed $\|\mathbf{u}-\mathcal{P}(\mathbf{u}_h)\|$ element velocities (ω=100).

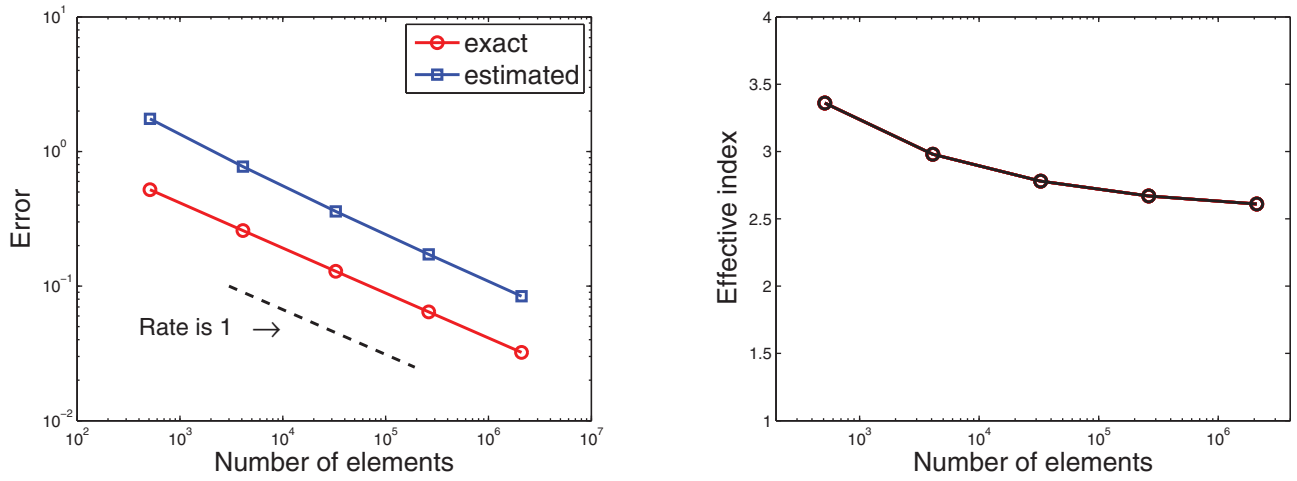

Fig. 5—Example 4: Estimated and actual velocity error (left) and the effective index (right).

and a given analytic solution

$$p(x,y,z) = \sin(\pi x)\sin(\pi y)\sin(\pi z).$$

In **Fig. 5,** we plot the exact error $\|\mathbf{u}-\mathbf{u}_h\|_a$ and the estimator $\|\mathbf{u}_h + K\nabla(\mathcal{I}_{OS}(\tilde{p}_h))\|_a + \eta_R$ vs. the number of gridblocks. The convergence rate of both the actual and estimated error is one. The estimator is larger than the actual error, and the effective index is measured by the ratio of the two. As the mesh is refined, the effective index approaches 2.5, which indicates the robustness of the estimator.

Example 5: Discontinuous Permeability. We consider a convergence test on a benchmark problem (3D Benchmark, Finite Volumes for Complex Applications VI) with a discontinuous permeability. The domain is a unit cube divided into the following four regions:

$$\mathrm{I} = \{(x,y,z) \in [0,1]^3 \, y \le 0.5 \text{ and } z \le 0.5\},$$

$$\mathrm{II} = \{(x,y,z) \in [0,1]^3 \, y > 0.5 \text{ and } z \le 0.5\},$$

$$\mathrm{III} = \{(x,y,z) \in [0,1]^3 \, y > 0.5 \text{ and } z > 0.5\},$$

$$\mathrm{IV} = \{(x,y,z) \in [0,1]^3 \, y \le 0.5 \text{ and } z > 0.5\}.$$

The permeability and pressure, respectively, are given as

$$K = \begin{cases} \mathrm{diag}(1,10,0.01) & \text{in I} \\ \mathrm{diag}(1,0.1,100) & \text{in II} \\ \mathrm{diag}(1,0.01,10) & \text{in III} \\ \mathrm{diag}(1,100,0.1) & \text{in IV} \end{cases}$$

$$p(x,y,z) = \begin{cases} 0.1\sin(2\pi x)\sin(2\pi y)\sin(2\pi z) & \text{in I} \\ 10\sin(2\pi x)\sin(2\pi y)\sin(2\pi z) & \text{in II} \\ 100\sin(2\pi x)\sin(2\pi y)\sin(2\pi z) & \text{in III} \\ 0.01\sin(2\pi x)\sin(2\pi y)\sin(2\pi z) & \text{in IV} \end{cases}$$

It is easy to check that the normal component of the velocity $\mathbf{u} = -K\nabla p$ is continuous across the interfaces. As in Example 1, the hexahedral meshes are generated by the following map:

$$x = \hat{x} + 0.05\sin(2\pi\hat{x})\cos(2\pi\hat{y})\cos(2\pi\hat{z}),$$

$$y = \hat{y} - 0.06\cos(2\pi\hat{x})\sin(2\pi\hat{y})\cos(2\pi\hat{z}),$$

$$z = \hat{z} + 0.07\cos(2\pi\hat{x})\cos(2\pi\hat{y})\sin(2\pi\hat{z}).$$

Fig. 6 presents such a mesh. As the theory predicts, we observe first-order convergence for both the face velocity and pressure in Fig. 6.

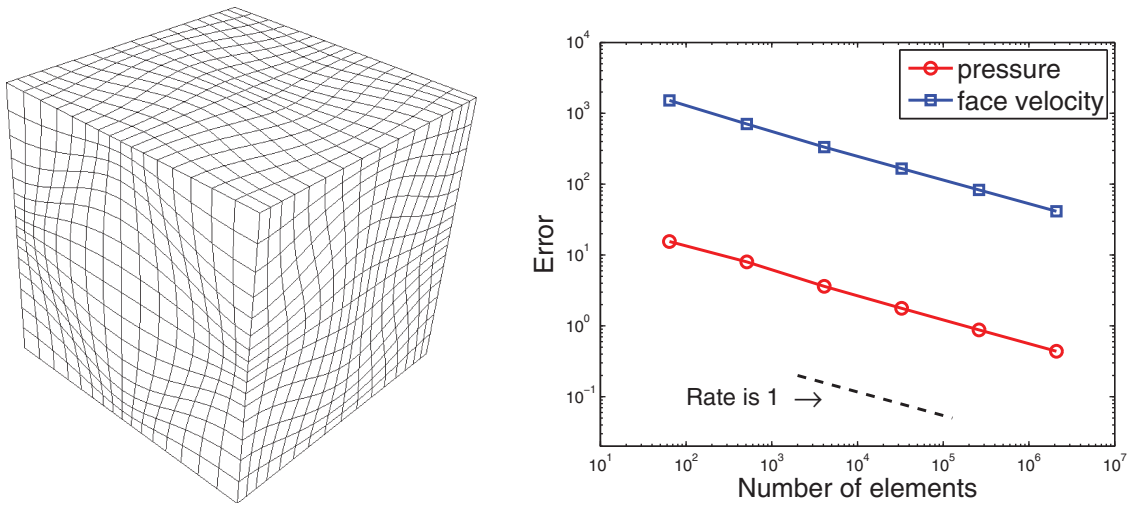

Fig. 6—Example 5: An h^2-perturbed hexahedral mesh (left), and the convergence (right) of the face-velocity error $\|\mathbf{u}-\mathbf{u}_h\|_{\mathcal{F}_h}$ and the pressure error $\|p-p_h\|$ for the nonsymmetric MFMFE method.

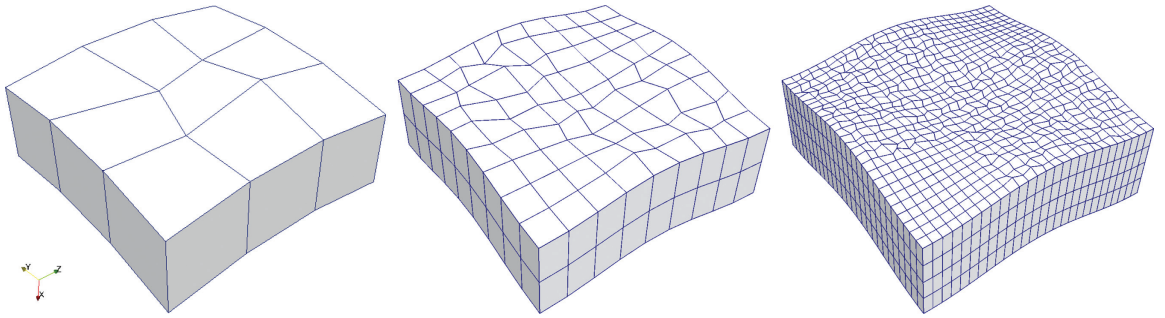

Fig. 7—Refinements of hexahedral gridblocks.

Computational Results for Slightly Compressible Single-Phase Flow

Slightly compressible single-phase flow in porous media is governed by the mass-conservation equation,

$$\frac{\partial}{\partial t}(\phi\rho) + \nabla \cdot \mathbf{u} = f, \quad \ldots\ldots\ldots\ldots\ldots\ldots\ldots\ldots (38)$$

and Darcy's law,

$$\mathbf{u} = -\rho\frac{K}{\mu}(\nabla p - \rho\mathbf{g}), \quad \ldots\ldots\ldots\ldots\ldots\ldots\ldots\ldots (39)$$

where $\mathbf{u}$ is the Darcy velocity, ϕ is the porosity, f is the source term, p is the pressure, K is the rock permeability, μ is the kinematic viscosity, and $\mathbf{g}$ is the gravitational vector. The density $\rho = \rho(p)$ is given by

$$\rho = \rho^{\text{ref}} e^{c(p-p^{\text{ref}})}, \quad \ldots\ldots\ldots\ldots\ldots\ldots\ldots\ldots (40)$$

where ρ^{ref} and p^{ref} are the reference density and pressure, respectively, and c is the compressibility constant. For convenience, we assume no-flow boundary conditions. The velocity space $V_h^0 \subset V_h$ is defined by

$$V_h^0 = \{\mathbf{v} \in V_h | \mathbf{v} \cdot \mathbf{n} = 0 \text{ on } \partial\Omega\}. \quad \ldots\ldots\ldots\ldots\ldots (41)$$

The source term is treated using the Peaceman correction (1978).

Let $0 = t_0 < t_1 < \ldots$, and $\tau^m = t_{m+1} - t_m$. We apply the backward Euler implicit time scheme and the nonsymmetric MFMFE for the space discretization. At time t_{m+1}, find $\mathbf{u}_h^{m+1} \in V_h^0$ and $p_h^{m+1} \in W_h$ such that

$$\phi\frac{\rho(p_h^{m+1}) - \rho(p_h^m)}{\tau^m} + (\nabla \cdot \mathbf{u}_h^{m+1}, w_h) = (q^{m+1}, w_h), \; w \in W_h, \quad \ldots\ldots\ldots\ldots (42)$$

$$\left(\frac{\mu}{\rho^{m+1}}K^{-1}\mathbf{u}_h^{m+1}, \mathbf{v}_h\right)_Q - (p_h^{m+1}, \nabla \cdot \mathbf{v}_h) - (\rho^{m+1}\mathbf{g}, \mathbf{v}_h) = 0, \; \forall \mathbf{v} \in V_h^0. \quad \ldots\ldots\ldots\ldots (43)$$

Newton's method is used to solve the nonlinear system of equations arising from Eqs. 42 and 43. The x-axis is along the vertical direction.

Example 1. The reservoir has a dimension of 300×900×900 ft. An injection well with a bottomhole pressure of 1,600 psi is placed between the coordinates $(0, 150, 150)$ and $(300, 150, 150)$, and a production well with a bottomhole pressure of 1,000 psi is placed between the coordinates $(0, 750, 750)$ and $(300, 750, 750)$. The wells are all fully perforated in each layer. The permeability is given as a diagonal tensor with values 50, 200, and 200 md in each direction. Initially, the reservoir pressure is given by a hydrostatic computation based on a pressure of 1,200 psi at the top.

We consider a sequence of mesh refinements given in **Fig. 7.** The initial mesh has $1 \times 3 \times 3$ gridblocks. We refine each element by a half along the x-axis and by a third in the other two directions. The finest level has approximately one million gridblocks $(16 \times 243 \times 243)$. The gridpoints around the two wells are generated by uniform refinements along the y- and z-axis. For the remaining points, the y–z coordinates are generated by randomly perturbing the gridpoints from uniform refinements. The x-coordinates of the gridpoints are generated by a smooth mapping:

$$x = \hat{x} + 30\cos\left(\frac{\pi y}{450}\right)\cos\left(\frac{\pi z}{450}\right),$$

where $\hat{x}$ is the x-coordinate of the gridpoint from the uniform refinement. Because the resulting hexahedral meshes are highly distorted, we employ the nonsymmetric MFMFE method introduced in the second section. **Fig. 8** shows the pressure and velocity field at Day 10 computed on a mesh with 3×21×21 gridblocks.

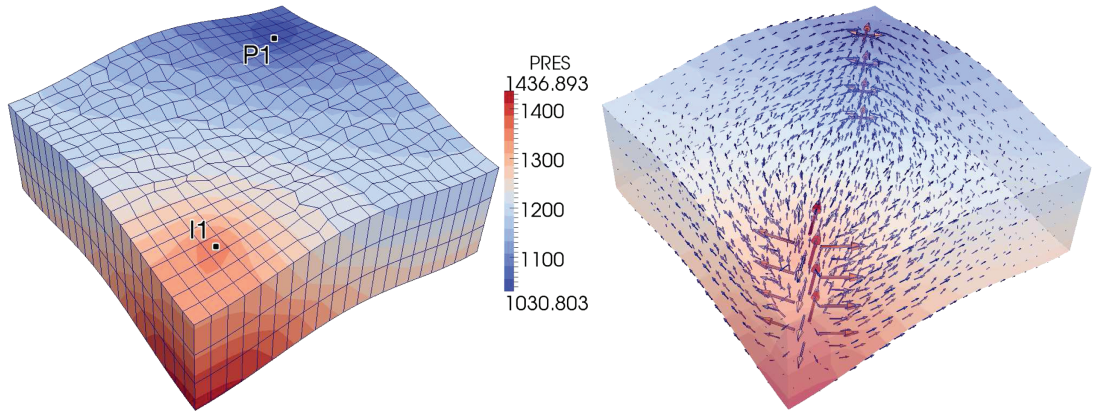

Fig. 8—Pressure (left) and velocity field (right) at Day 10.

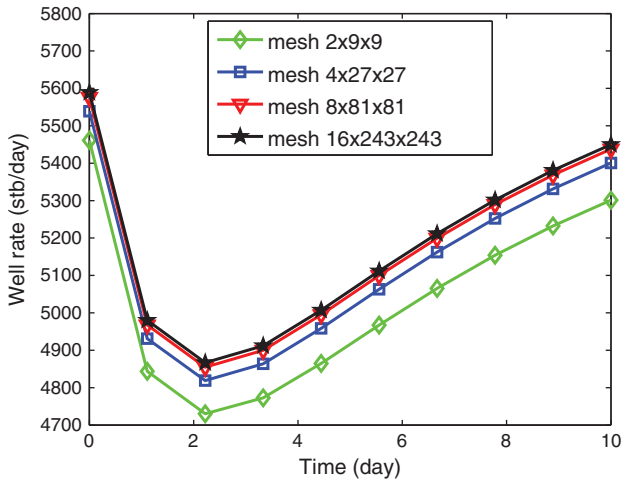

Fig. 9—Convergence of total production rate.

In **Fig. 9,** we report the total production rates under the different mesh refinements. We use the total production rate obtained on the finest level (16×243×243) as a reference solution. As the grids are refined, we clearly observe convergence of the total production rates to the reference curve.

The resulting linear algebraic system is solved using the software HYPRE (high-performance preconditioners) developed by researchers at Lawrence Livermore National Laboratory (https://computation.llnl.gov/casc/hypre/software.html). Specifically, we use the generalized minimum residual (GMRES) method with an algebraic multigrid method as a preconditioner. The stopping criteria for GMRES is relative residual less than 10^{-9}. The numbers of iterations reported in **Table 1** indicate the robustness of the solver with respect to refining the mesh.

Example 2. In this example, we illustrate the ability of the MFMFE method to simulate flow on realistic irregular geometries and heterogeneous media. We consider a hexahedral mesh; porosity; and x-, y-, and z- permeability fields from the Brugge benchmark project (Peters et al. 2010) **(Fig. 10).** Both the permeabilities and the porosity are highly heterogeneous. As with Example 1, the pressure is initially given by the hydrostatic computation with 1,500 psi at the top of the reservoir. We specify three injection wells with bottomhole pressure of 2,600 psi and eight production wells with bottomhole pressure of 1,000 psi. The well locations are indicated in **Fig. 11.** The pressure field for Days 10 and 100 is also shown in Fig. 11.

Computational Results for Two-Phase Flow

We describe the incompressible two-phase-flow equations. Let α denote either a wetting phase w or a nonwetting phase n. The mass-conservation equation for the phase α reads

$$\frac{\partial}{\partial t}(\phi s_\alpha) + \nabla \cdot \mathbf{u}_\alpha = q_\alpha,\ \alpha = w, n, \quad \ldots\ldots\ldots\ldots\ldots\ldots (44)$$

where ϕ is the porosity, s_α is the phase saturation, and q_α is a source or sink term. The phase velocity $\mathbf{u}_\alpha$ is given by Darcy's law:

$$\mathbf{u}_\alpha = -\lambda_\alpha K(\nabla p_\alpha - \rho_\alpha \mathbf{g}), \quad \ldots\ldots\ldots\ldots\ldots\ldots\ldots\ldots (45)$$

where K is the permeability, p_α is the phase pressure, and ρ_α is the phase density. The phase mobility λ_α is defined as

$$\lambda_\alpha(s_\alpha) = \frac{k_{r\alpha}(s_\alpha)}{\mu_\alpha}, \quad \ldots\ldots\ldots\ldots\ldots\ldots\ldots\ldots\ldots (46)$$

where μ_α is the dynamic viscosity and $k_{r\alpha}$ is the relative permeability. Also, the saturations satisfy the volume-balance equation,

$$s_w + s_n = 1, \quad \ldots\ldots\ldots\ldots\ldots\ldots\ldots\ldots\ldots\ldots (47)$$

and the capillary pressure is defined by

$$p_c = p_n - p_w. \quad \ldots\ldots\ldots\ldots\ldots\ldots\ldots\ldots\ldots\ldots (48)$$

The capillary pressure is usually a function of the wetting-phase saturation determined by experiments.

Define the total velocity $\mathbf{u}_t$ and the total mobility λ_t as

$$\mathbf{u}_t = \mathbf{u}_w + \mathbf{u}_n,\ \lambda_t = \lambda_w + \lambda_n. \quad \ldots\ldots\ldots\ldots\ldots\ldots (49)$$

Using Eq. 45, the total velocity can be expressed as

$$\mathbf{u}_t = -\lambda_t K\left(\nabla p_w - \rho_w \mathbf{g} + \frac{\lambda_n}{\lambda_t}(\nabla p_c - (\rho_n - \rho_w)\mathbf{g})\right). \quad \ldots\ldots\ldots\ldots\ldots\ldots (50)$$

TABLE 1—AVERAGE NUMBERS OF GMRES ITERATIONS WITH AMG PRECONDITIONER

Mesh	$2 \times 9 \times 9$	$4 \times 27 \times 27$	$8 \times 81 \times 81$	$16 \times 243 \times 243$
Iterations	5	6	7	8

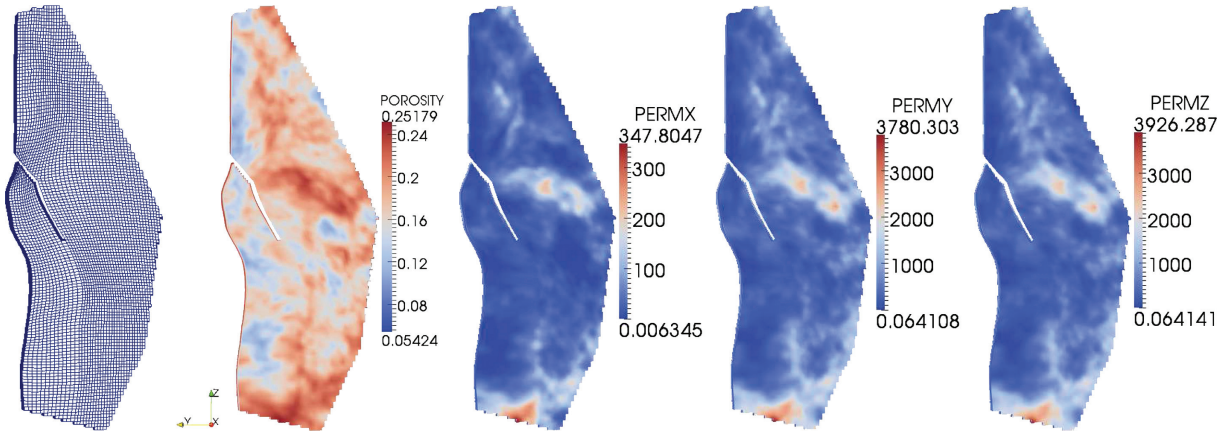

Fig. 10—Brugge data set: mesh, porosity, and permeabilities.

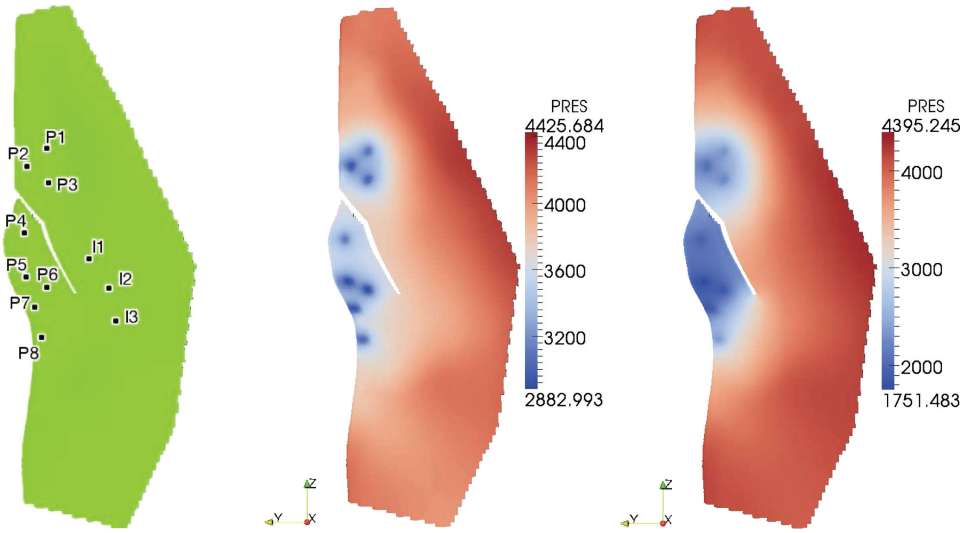

Fig. 11—Well locations (left), pressure at Day 10 (middle), and pressure at Day 100 (right).

Summing Eq. 44 for the two phases gives

$$\nabla \cdot \mathbf{u}_t = q_w + q_n. \quad \ldots\ldots\ldots\ldots\ldots\ldots\ldots\ldots (51)$$

The primary variables are chosen to be the wetting-phase pressure p_w and the wetting-phase saturation s_w. Then, Eq. 51 and the wetting-phase equation (Eq. 44) give a closed system of equations with an initial condition,

$$s_w(x,0) = s_0, \quad \ldots\ldots\ldots\ldots\ldots\ldots\ldots\ldots (52)$$

and a no-flow boundary condition for the total velocity,

$$\mathbf{u}_t \cdot \mathbf{n} = 0 \text{ on } \partial\Omega. \quad \ldots\ldots\ldots\ldots\ldots\ldots\ldots\ldots (53)$$

We use an iterative coupling approach (Lu 2008; Wheeler and Xue 2010) to solve the pressure and saturation equations. At each timestep, we first solve the wetting-phase pressure equation given by Eqs. 50 and 51 using the latest saturation values, and then solve Eq. 44 with $\alpha = w$. The pressure equation is solved implicitly, while the saturation is solved explicitly. The timestep for the saturation is chosen to satisfy the CFL condition. As a result, the timestep size for the saturation could be smaller than the pressure's size. The iteration is then repeated until the relative error of local mass balances is smaller than a given tolerance. **Fig. 12** presents a flow chart of the iterative coupling.

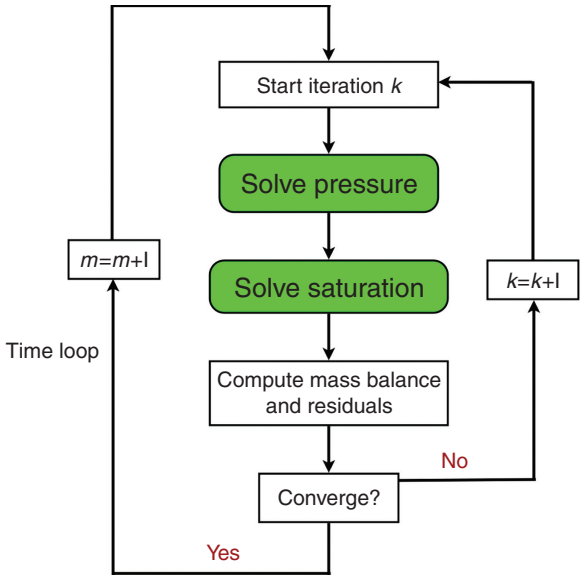

Fig. 12—Flow chart of iterative coupling.

More precisely, at timestep $m+1$ and iterative coupling step $k+1$,

$$\mathbf{u}_t^{m+1,k+1} = -\lambda_t^{m+1,k} K\left(\nabla p_w^{m+1,k+1} + F(p_w^{m+1,k}, s_w^{m+1,k})\right), \quad \ldots\ldots\ldots\ldots\ldots\ldots (54)$$

$$\nabla \cdot \mathbf{u}_t^{m+1,k+1} = q_w^{m+1,k} + q_n^{m+1,k}, \quad \ldots\ldots\ldots\ldots\ldots\ldots (55)$$

where

$$F(p_w, s_w) := -\rho_w \mathbf{g} + \frac{\lambda_n}{\lambda_t}(\nabla p_c - (\rho_n - \rho_w)\mathbf{g}).$$

The saturation equation is solved explicitly; that is, for given $p_w^{m+1,k+1}$ and $s_w^{m+1,k}$, $s_w^{m+1,k+1}$ satisfies

$$\phi \frac{s_w^{m+1,k+1} - s_w^m}{\tau^m} = G(p_w^{m+1,k+1}, s_w^{m+1,k}), \quad \ldots\ldots\ldots\ldots\ldots\ldots (56)$$

where

$$G(p_w, s_w) := q_w - \nabla \cdot \mathbf{u}_w.$$

We apply the MFMFE method to discretize Eqs. 54 and 55: find $p_w^{m+1,k+1}$ and $\mathbf{u}_t^{m+1,k+1}$, with given $s_w^{m+1,k}$, such that

$$\left(\frac{1}{\lambda_t^{m+1,k}} K^{-1} \mathbf{u}_t^{m+1,k+1}, \mathbf{v}\right)_Q - (p_w^{m+1,k+1}, \nabla \cdot \mathbf{v}) = \left(F(p_w^{m+1,k}, s_w^{m+1,k}), \mathbf{v}\right), \forall \mathbf{v} \in V_h^0, \quad \ldots\ldots\ldots\ldots\ldots\ldots (57)$$

$$(\nabla \cdot \mathbf{u}_t^{m+1,k+1}, w) = (q_w^{m+1,k} + q_n^{m+1,k}, w), \forall w \in W_h. \quad \ldots (58)$$

Recall that the MFMFE method gives a cell-centered scheme for the pressure, because $\mathbf{u}_t^{m+1,k+1}$ has a local flux representation in terms of $p_w^{m+1,k+1}$. Thus, one does not need to solve a saddle-point system.

Next, on the basis of $p_w^{m+1,k+1}$, $\mathbf{u}_w^{m+1,k+1}$, and $s_w^{m+1,k}$, we apply a discontinuous Galerkin (DG) method and explicit forward Euler method for the wetting-phase saturation (Eq. 56). The timestep size is chosen to satisfy the CFL condition. In the numerical experiments discussed in earlier subsections, the lowest-order DG method, equivalent to a finite-volume method, with upwinding is used.

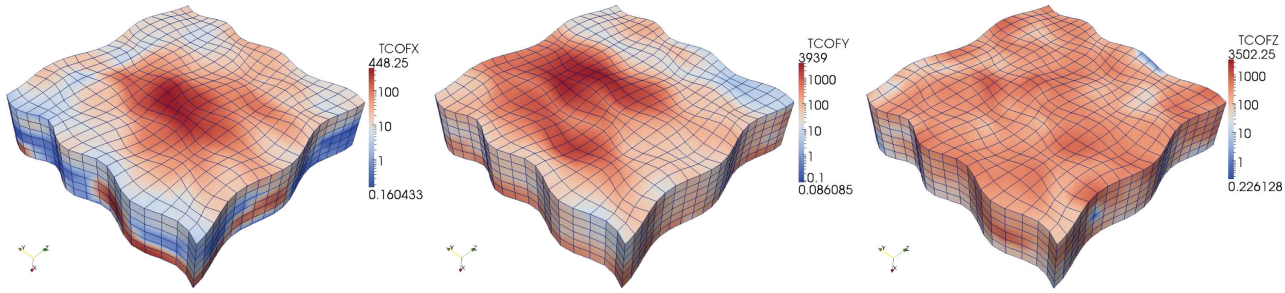

Fig. 13—Upscaled SPE10 permeability along the *x*-direction (left), the *y*-direction (middle), and the *z*-direction (right).

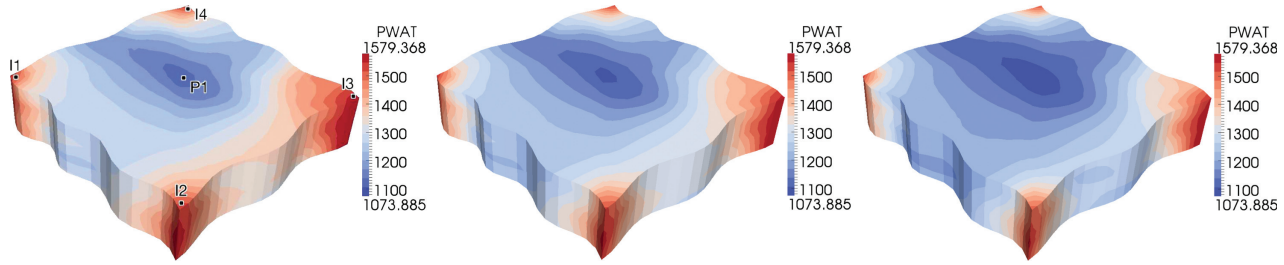

Fig. 14—Pressure field at Days 50, 100, and 200.

In the following examples, the relative permeability of the wetting and nonwetting phases is given as

$$K_{rw} = 0.9s_e^2, k_{rn} = 0.5(1 - s_e)^2,$$

where s_e is the effective saturation,

$$s_e = \frac{s_w - s_{rw}}{1 - s_{rw} - s_{rn}}, \; s_{rw} \le s_w \le 1 - s_{rn}.$$

Here, s_{rw} is the residual wetting-phase saturation and s_{rn} is the residual nonwetting-phase saturation.

In the following examples, the residual saturations are chosen as $s_{rw} = 0.2$ and $s_{rn} = 0.05$. The iterative coupling stopping criteria is that the local mass-balance errors for both the wetting and nonwetting phases are smaller than 10^{-4}. A uniform porosity is chosen as 20%. The x-axis is along the vertical direction.

Example 1: Upscaled SPE10 Permeability on a Hexahedral Mesh. This example is a 3D two-phase oil-/water-flow problem with general hexahedral gridblocks and with upscaled SPE10 permeability. The maximum dimensions of the reservoir are 96×400×400 ft. The computational grid is 6×20×20. Harmonic average is used in the upscaling of the permeability (see **Fig. 13** for the permeability in the three directions). The permeability is highly heterogeneous, with six-order-of-magnitude jumps.

Four injection wells are located at the four corner gridblocks. A production well is placed at the center of the reservoir. The bottomhole pressures at the injection wells and the production well are kept constant at 1,600 psi and 1,000 psi, respectively.

Initially, the reservoir has constant water-phase saturation $s_w = 0.2$. Given this initial saturation, the pressure field at $t = 0$ is determined by solving the nonlinear steady equation (Eqs. 50 and 51) with a no-flow boundary condition (Eq. 53). In this example, the gravity and capillary effects are ignored.

The total simulation time is 200 days. **Figs. 14 and 15** show the pressure and saturation profiles, repectively, at Days 50, 100, and 200. Clearly the flow is directed from the four corners to the center with preferential directions within the high-permeability zones.

Example 2: Heterogeneous Capillary Effect. In this example, we consider a heterogeneous capillary effect in two-phase flow. The reservoir consists of two different rock types (see **Fig. 16**). Rock Type 1 has a low permeability of 52.6 md. Rock Type 2 has a high permeability of 504 md. We employ a modified Brooks-Corey function for modeling heterogeneous capillary pressures:

$$p_c(s_e) = \begin{cases} p_d s_{c1}^{-\frac{1}{\lambda}} & \text{if } 0 \le s_e < s_{c1}, \\ p_d s_e^{-\frac{1}{\lambda}} & \text{if } s_{c1} \le s_e \le s_{c2}, \\ p_d s_{c2}^{-\frac{1}{\lambda}} \dfrac{1 - s_e}{1 - s_{c2}} & \text{if } s_{c2} < s_e \le 1, \end{cases} \quad \ldots\ldots\ldots (59)$$

where the cutoff saturations s_{c1} and s_{c2} are chosen as 0.01 and 0.9, respectively. The displacement pressure p_d and the pore-size-distribution index λ are given in **Table 2.** See Fig. 16 for the

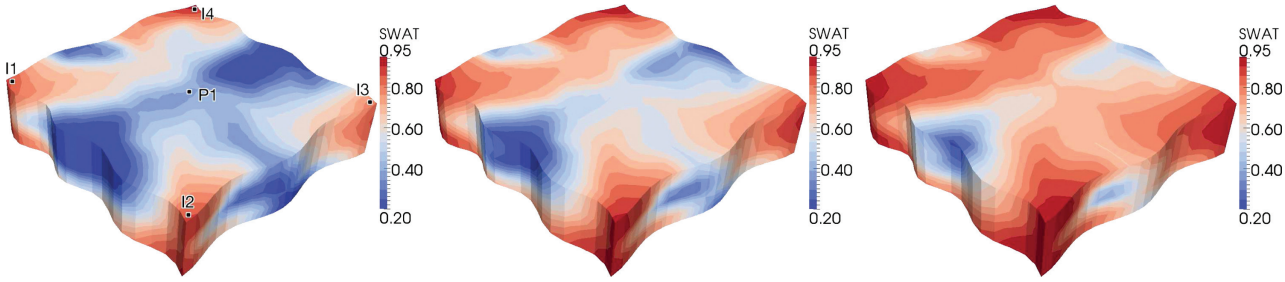

Fig. 15—Water-saturation field at Days 50, 100, and 200.

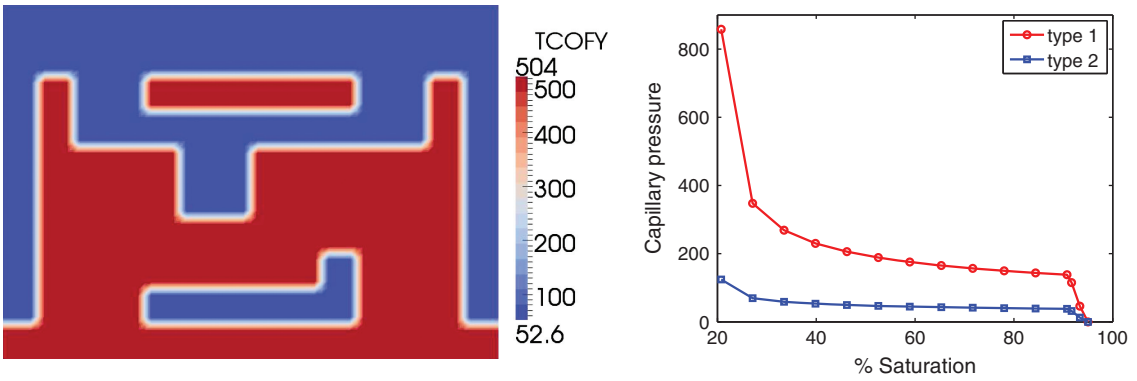

Fig. 16—Permeability (left) and capillary pressure curves (right).

TABLE 2—DISPLACEMENT PRESSURE AND PORE-SIZE DISTRIBUTION INDEX

Rock Type	p_d	λ
Type 1	135	2.49
Type 2	37.7	3.86

capillary pressure curves for different rock types. In this example, the gravity effect is ignored.

The computational domain is 700×500 ft. The origin of the x–y coordinate system is located at the bottom left corner. The problem consists of 3,500 gridblocks, with 70 gridblocks along the x-direction and 50 along the y-direction. There are two injection wells and 10 production wells. The injection wells are located near the top of the reservoir at coordinates $(345, 495)$ and $(355, 495)$. Five production wells are located along each side. The x-coordinates of the left- and the right-side wells are 25 and 675, respectively. The y-coordinates for each side are 25, 125, 225, 325, and 425. The reservoir contains water and oil. Initially, the water saturation is 20%. Water is injected at bottomhole pressure of 1,600 psi. The bottomhole pressure at the production wells is 1,000 psi.

We run simulations for two cases—with and without capillary effects. **Fig. 17** shows the water-saturation profiles when ignoring the capillary pressure. In this case, the front is very diffused. **Fig. 18** shows strong capillary effects. Water is injected from the low-permeability rock. When the water front first reaches the interface between low- and high-permeability rocks, it cannot penetrate into the high-permeability rock. This is because of the dominance of the capillary pressure at low water saturation. As water builds up at the interface, the capillary pressures become smaller and the water starts to invade the high-permeability zone. Similarly, the capillary pressure causes water in the high-permeability zone to invade easily the low-permeability zone. Note that the saturation is discontinuous across the interfaces because of the different capillary pressure curves in the two rocks.

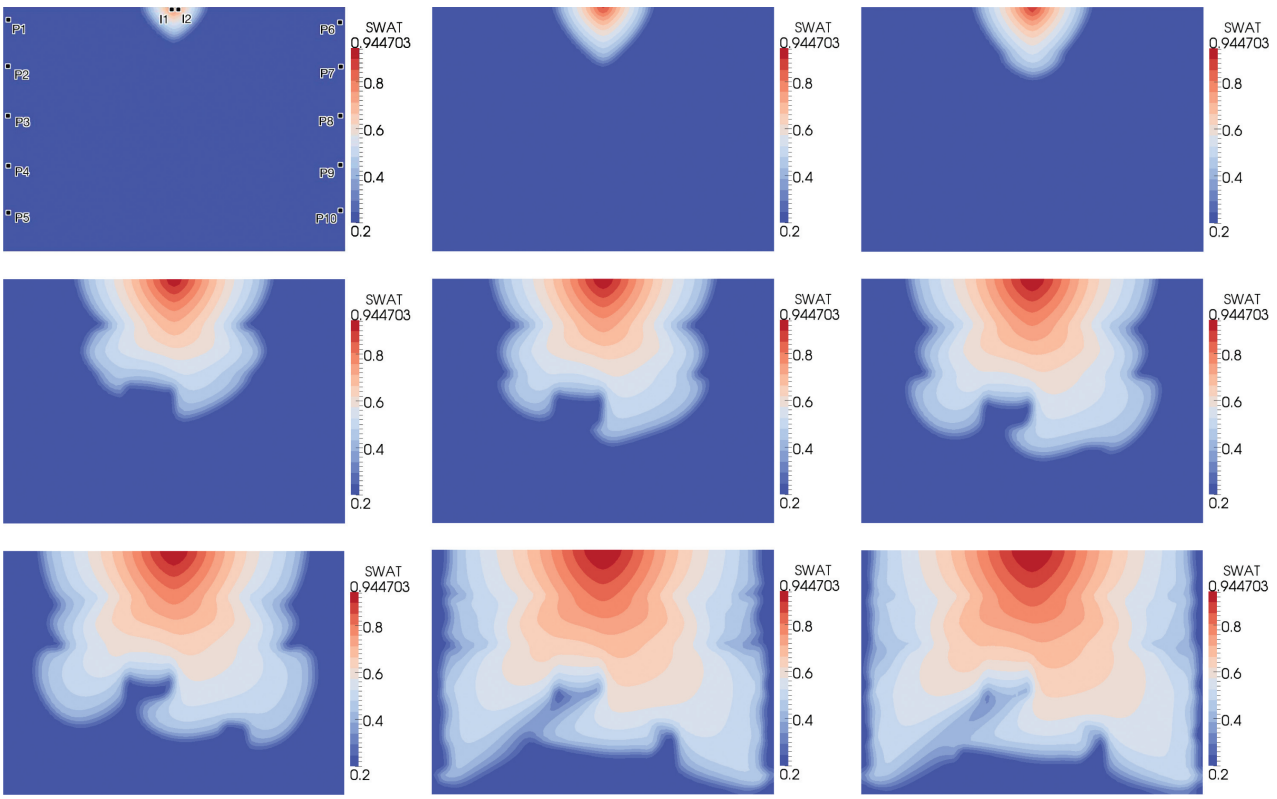

Fig. 17—Zero capillary pressure: Water saturation at Days 6, 14, 20, 58, 76, 94, 110, 158, and 178.

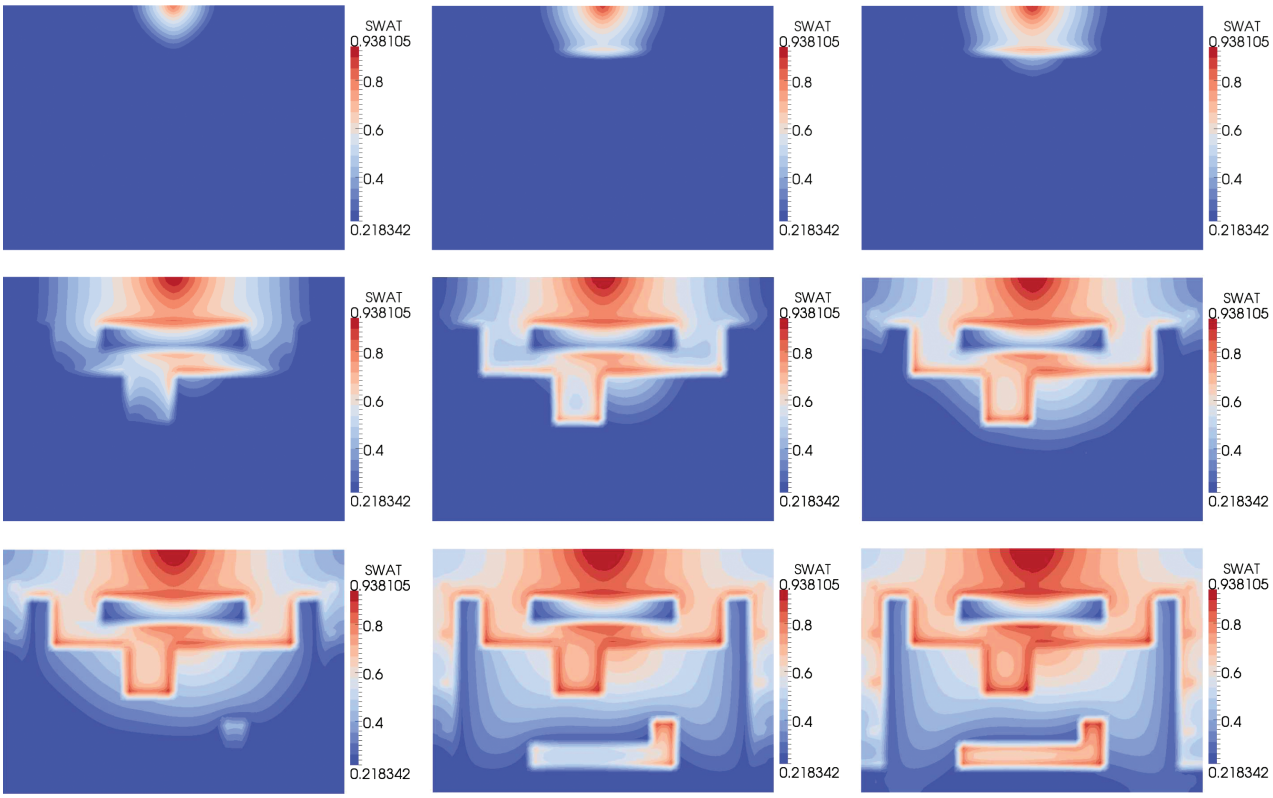

Fig. 18—With capillary pressure: Water saturation at Days 6, 14, 20, 58, 76, 94, 110, 158, and 178.

Conclusions

We presented an accurate and efficient cell-centered discretization method, the MFMFE method, for Darcy flow on general hexahedral and simplicial grids. The method exhibits first-order convergence on rough grids and second-order convergence on smooth grids. The method has been extended to solving the pressure equation in a two-phase-flow system, coupled with a DG method for the saturation equation. Local post-processing can be applied to obtain accurate velocities in the interior of the gridblocks needed for higher-order transport. The variational formulation of the method allows for multiscale and multiphysics extensions. Employing *a posteriori* error estimation and efficient preconditioners for the algebraic system leads to a robust computational framework that provides accurate approximations of complex flows in highly heterogeneous media.

Nomenclature

d = dimension
DF_E = Jacobian matrix
e = edge in 2D and face in 3D
E = gridblock
f,q = external source
F_E = mapping from reference to physical gridblock
$\mathbf{g}$ = gravitational constant vector
J_E = determinant of Jacobian matrix
$k_{r\alpha}$ = relative permeability of phase α
K = permeability tensor
n = nonwetting phase
$\mathbf{n}$ = unit normal vector
p = pressure
p_c = capillary pressure
p_d = entry pressure
P_0,P_1 = polynomial spaces of order 0 and 1
$\mathcal{P}$ = post-processing operator
Q_h = interpolation operator
$\mathbb{R}$ = Cartesian space
s = saturation
s_{rn} = residual saturation for non-wetting phase n
s_{rw} = residual saturation for wetting phase w
t = time
T_h = partition of the domain
$\boldsymbol{u}$ = darcy velocity
$\boldsymbol{u_t}$ = total velocity
v, $\boldsymbol{q}$,w = test functions
V_h, W_h = finite-element spaces
w = wetting phase
α = phase
λ_α = mobility of phase α
λ_t = total mobility
μ = viscosity
$\mathbf{\Pi}$ = interpolation operator
ρ = density
τ = timestep size
ϕ = porosity
$\mathbf{\Omega}$ = domain of the problem

Subscripts

$\mathcal{F}_h$ = face norm
h = characteristic mesh size
n = nonwetting phase
Q = numerical quadrature
w = wetting phase
α = phase

Superscripts

d = dimension
E = gridblock
m, k = integer indicies

Acknowledgments

Mary F. Wheeler is supported by the NSF-CDI under contract number DMS 0835745, DOE grant DE-FG02-04ER25617, and the Center for Frontiers of Subsurface Energy Security under Contract No. DE-SC0001114. Guangri Xue is supported by

Award No. KUS-F1-032-04, made by the King Abdullah University of Science and Technology. Ivan Yotov is partially supported by the DOE grant DE-FG02-04ER25618, the NSF grant DMS 0813901, and the J. Tinsley Oden Faculty Fellowship, Institute for Computational Engineering and Sciences, University of Texas at Austin.

References

Aavatsmark, I. 2002. An Introduction to Multipoint Flux Approximations for Quadrilateral Grids. *Comput. Geosci.* **6** (3–4): 405–432. http://dx.doi.org/10.1023/A:1021291114475.

Aavatsmark, I., Barkve, T., and Mannseth, T. 1998b. Control-Volume Discretization Methods for 3D Quadrilateral Grids in Inhomogeneous, Anisotropic Reservoirs. *SPE J.* **3** (2): 146–154. SPE-38000-PA. http://dx.doi.org/10.2118/38000-PA.

Aavatsmark, I., Barkve, T., Bøe, Ø., and Mannseth, T. 1998a. Discretizaton on unstructured grids for inhomogeneous, anisotropic media. Part II: Discussion And Numerical Results. *SIAM J. Sci. Comput.* **19** (5): 1717–1736. http://dx.doi.org/10.1137/S1064827595293594.

Aavatsmark, I., Eigestad, G.T., Heimsund, B.-O., Mallison, B., Nordbotten, J.M., and Øian, E. 2010. A New Finite-Volume Approach to Efficient Discretization on Challenging Grids. *SPE J.* **15** (3): 658–669. SPE-106435-PA. http://dx.doi.org/10.2118/106435-PA.

Aavatsmark, I., Eigestad, G.T., Klausen, R.A., Wheeler, M.F., and Yotov, I. 2007. Convergence of a symmetric MPFA method on quadrilateral grids. *Comput. Geosci.* **11** (4): 333–345. http://dx.doi.org/10.1007/s10596-007-9056-8.

Aavatsmark, I., Eigestad, G.T., Mallison, B.T., and Nordbotten, J.M. 2008. A compact multipoint flux approximation method with improved robustness. *Numerical Methods for Partial Differential Equations* **27** (5): 1329–1360. http://dx.doi.org/10.1002/num.20320.

Arbogast, T., Cowsar, L.C., Wheeler, M.F., and Yotov, I. 2000. Mixed Finite Element Methods on Nonmatching Multiblock Grids. *SIAM J. Numer. Anal.* **37** (4): 1295–1315. http://dx.doi.org/10.1137/s0036142996308447.

Arbogast, T., Pencheva, G., Wheeler, M.F., and Yotov, I. 2007. A Multiscale Mortar Mixed Finite Element Method. *Multiscale Modeling & Simulation* **6** (1): 319–346. http://dx.doi.org/10.1137/060662587.

Brezzi, F., Douglas, J., and Marini, L.D. 1985. Two families of mixed finite elements for second order elliptic problems. *Numerische Mathematik* **47** (2): 217–235. http://dx.doi.org/10.1007/bf01389710.

Brezzi, F., Douglas, J., Durán, R., and Fortin, M. 1987. Mixed finite elements for second order elliptic problems in three variables. *Numerische Mathematik* **51** (2): 237–250. http://dx.doi.org/10.1007/bf01396752.

Brezzi, F., Fortin, M. and Marini L. D. 2006. Error analysis of piecewise constant pressure approximations of Darcy's law. *Comput. Methods Appl. Mech. Eng.* (**195**), 1547–1559.

Ciarlet, P.G. 2002. *The Finite Element Method for Elliptic Problems*, second edition, No. 40. Philadelphia, Pennsylvania: Classics in Applied Mathematics, SIAM.

Edwards, M.G. 2002. Unstructured, Control-Volume Distributed, Full-Tensor Finite Volume Schemes with Flow Based Grids. *Comput. Geosci.* **6** (3–4): 433–452. http://dx.doi.org/10.1023/A:1021243231313.

Edwards, M.G. 2006. Higher-resolution hyperbolic-coupled-elliptic flux-continuous CVD schemes on structured and unstructured grids in 3-D. *Int. J. Numer. Methods Fluids* **51** (9–10): 1079–1095. http://dx.doi.org/10.1002/fld.1289.

Edwards, M.G. and Pal, M. 2008. Positive-definite q-families of continuous subcell Darcy-flux CVD(MPFA) finite-volume schemes and the mixed finite element method. *Int. J. Numer. Methods Fluids* **57** (4): 355–387. http://dx.doi.org/10.1002/fld.1586.

Edwards, M.G. and Rogers, C.F. 1998. Finite volume discretization with imposed flux continuity for the general tensor pressure equation. *Comput. Geosci.* **2** (4): 259–290. http://dx.doi.org/10.1023/A:1011510505406.

Edwards, M.G. and Zheng, H. 2008. A quasi-positive family of continuous Darcy-flux finite-volume schemes with full pressure support. *J. Comput. Phys.* **227** (22): 9333–9364. http://dx.doi.org/10.1016/j.jcp.2008.05.028.

Edwards, M.G. and Zheng, H. 2010. Double-families of quasi-positive Darcy-flux approximations with highly anisotropic tensors on structured and unstructured grids. *J. Comput. Phys.* **229** (3): 594–625. http://dx.doi.org/10.1016/j.jcp.2009.09.037.

Edwards, M.G. and Zheng, H. 2011. Quasi M-Matrix Multifamily Continuous Darcy-Flux Approximations with Full Pressure Support on Structured and Unstructured Grids in Three Dimensions. *SIAM Journal on Scientific Computing* **33** (2): 455–487. http://dx.doi.org/10.1137/080745390.

Falk, R.S., Gatto, P., and Monk, P. 2011. Hexahedral $H(\mathrm{div})$ and $H(\mathrm{curl})$ finite elements. *ESAIM: Mathematical Modelling and Numerical Analysis* **45** (01): 115–143. http://dx.doi.org/doi:10.1051/m2an/2010034.

Friis, H.A., Edwards, M.G., and Mykkeltveit, J. 2008. Symmetric Positive Definite Flux-Continuous Full-Tensor Finite-Volume Schemes on Unstructured Cell-Centered Triangular Grids. *SIAM Journal on Scientific Computing* **31** (2): 1192–1220. http://dx.doi.org/10.1137/070692182.

Ganis, B. and Yotov, I. 2009. Implementation of a mortar mixed finite element method using a Multiscale Flux Basis. *Comput. Meth. Appl. Mech. Eng.* **198** (49–52): 3989–3998. http://dx.doi.org/10.1016/j.cma.2009.09.009.

Hoteit, H. and Firoozabadi, A. 2008. Numerical modeling of two-phase flow in heterogeneous permeable media with different capillarity pressures. *Adv. Water Resour.* **31** (1): 56–73. http://dx.doi.org/10.1016/j.advwatres.2007.06.006.

Ingram, R., Wheeler, M.F., and Yotov, I. 2010. A Multipoint Flux Mixed Finite Element Method on Hexahedra. *SIAM J. Numer. Anal.* **48** (4): 1281–1312. http://dx.doi.org/10.1137/090766176.

Klausen, R.A. and Winther, R. 2006a. Convergence of multipoint flux approximations on quadrilateral grids. *Numerical Methods for Partial Differential Equations* **22** (6): 1438–1454. http://dx.doi.org/10.1002/num.20158.

Klausen, R.A. and Winther, R. 2006b. Robust convergence of multi point flux approximation on rough grids. *Numerische Mathematik* **104** (3): 317–337. http://dx.doi.org/10.1007/s00211-006-0023-4.

Klausen, R.A., Radu, F.A., and Eigestad, G.T. 2008. Convergence of MPFA on triangulations and for Richards' equation. *Int. J. Numer. Methods Fluids* **58** (12): 1327–1351. http://dx.doi.org/10.1002/fld.1787.

Lamine, S. and Edwards, M.G. 2010. Higher Order Multidimensional Upwind Convection Schemes for Flow in Porous Media on Structured and Unstructured Quadrilateral Grids. *SIAM J. Sci. Comput.* **32** (3): 1119–1139. http://dx.doi.org/10.1137/080727750.

Lipnikov, K., Shashkov, M., and Yotov, I. 2009. Local flux mimetic finite difference methods. *Numerische Mathematik* **112** (1): 115–152. http://dx.doi.org/10.1007/s00211-008-0203-5.

Lu, B. 2008. *Iteratively coupled reservoir simulation for multiphase flow in porous media*. PhD dissertation, The University of Texas at Austin, Austin, Texas (December 2008).

Naff, R.L., Russell, T.F., and Wilson, J.D. 2002. Shape Functions for Velocity Interpolation in General Hexahedral Cells. *Comput. Geosci.* **6** (3): 285–314. http://dx.doi.org/10.1023/a:1021218525861.

Peaceman, D.W. 1978. Interpretation of Well-Block Pressures in Numerical Reservoir Simulation. *SPE J.* **18** (3): 183–194. SPE-6893-PA. http://dx.doi.org/10.2118/6893-PA.

Pencheva, G., Vohralík, M., Wheeler, M., and Wildey, T. 2010. Robust a posteriori error control and adaptivity for multiscale, multinumerics, and mortar coupling. Technical Report 10-15, University of Texas at Austin, Institute for Computational Engineering and Sciences (ICES), Austin, Texas.

Peters, L., Arts, R.J., Brouwer, G.K., et al. 2010. Results of the Brugge Benchmark Study for Flooding Optimization and History Matching. *SPE Res Eval & Eng* **13** (3): 391–405. SPE-119094-PA. http://dx.doi.org/10.2118/119094-PA.

Vohralík, M. 2006. Equivalence between lowest-order mixed finite element and multi-point finite volume methods on simplicial meshes. *ESAIM: Mathematical Modelling and Numerical Analysis* **40** (02): 367–391. http://dx.doi.org/doi:10.1051/m2an:2006013.

Wheeler, J.A., Wheeler, M.F., and Yotov, I. 2002. Enhanced Velocity Mixed Finite Element Methods for Flow in Multiblock Domains. *Comput. Geosci.* **6** (3): 315–332. http://dx.doi.org/10.1023/a:1021270509932.

Wheeler, M., Xue, G., and Yotov, I. 2012a. Local velocity postprocessing for multipoint flux methods on general hexahedra. *Int. J. Numer. Anal. Model.* **9**(3): 607–627.

Wheeler, M.F. and Xue, G. 2010. Accurate Locally Conservative Discretizations for Modeling Multiphase Flow in Porous Media on General Hexahedra Grids. Presented at the 12th European Conference on the Mathematics of Oil Recovery (ECMOR XII), Oxford, UK, Sep. 6–9.

Wheeler, M.F. and Yotov, I. 2006. A multipoint flux mixed finite element method. *SIAM J. Sci. Comput.* **44** (5): 2082–2106. http://dx.doi.org/10.1137/050638473.

Wheeler, M.F., Wildey, T., and Xue, G. 2010a. Efficient algorithms for multiscale modeling in porous media. *Numerical Linear Algebra with Applications* **17** (5): 771–785. http://dx.doi.org/10.1002/nla.742.

Wheeler, M.F., Wildey, T., and Yotov, I. 2011. A multiscale preconditioner for stochastic mortar mixed finite elements. *Comput. Meth. Appl. Mech. Eng.* **200** (9–12): 1251–1262. http://dx.doi.org/10.1016/j.cma.2010.10.015.

Wheeler, M.F., Xue, G., and Yotov, I. 2012b. A multipoint flux mixed finite element method on distorted quadrilaterals and hexahedra. *Numerische Mathematik* **121** (1): 165-204.

Wheeler, M.F., Xue, G., and Yotov, I. 2012c. A multiscale mortar multipoint flux mixed finite element method. *Mathematical Modeling and Numerical Analysis* **46** (4): 759-796. http://dx.doi.org/10.1051/m2an/2011064.

Younes, A. and Fontaine, V. 2008. Hybrid and multi-point formulations of the lowest-order mixed methods for Darcy's flow on triangles. *Int. J. Numer. Methods Fluids* **58** (9): 1041–1062. http://dx.doi.org/10.1002/fld.1785.

Mary Wheeler is a professor of aerospace engineering and engineering mechanics, as well as a professor of petroleum and geosystems engineering, at the University of Texas, as well as the Director of the Center for Subsurface Modeling at that institution. Wheeler's research interests include numerical solution of partial differential systems with application to the modeling of subsurface and surface flows and parallel computation. Wheeler holds BA and MA degrees, both in mathematics, from the University of Texas at Austin and a PhD degree in mathematics from Rice University.

Guangri Xue is a research scientist at Shell International Exploration and Production. Prior to joining Shell, he worked at the Institute for Computational Engineering and Sciences at the University of Texas at Austin as a research associate, and worked at the Lawrence Livermore National Laboratory as a visiting scientist on scalable algebraic multigrid solvers for computational fuel-cell dynamics. His specialization includes reservoir simulation, advanced discretization, upscaling and multiscale modeling, and solvers. He holds a PhD degree in applied and computational mathematics from the Pennsylvania State University.

Ivan Yotov is Professor and Chair of the Department of Mathematics at the University of Pittsburgh. His research interests are in numerical analysis of partial differential equations and large-scale scientific computing with applications to flow in porous media, computational fluid dynamics, and biomedical problems. His recent work spans stochastic modeling and uncertainty quantification, multiscale modeling of multiphysics systems, advanced discretizations, scalable parallel algorithms, and adaptive mesh-refinement methods. He held a postdoctoral position at the Institute for Computational Engineering and Sciences at the University of Texas at Austin before joining the University of Pittsburgh in 1998. He has authored or co-authored more than 60 scientific papers. Yotov holds a PhD degree in computational and applied mathematics from Rice University.